

North Atlantic forcing of tropical Indian Ocean climate

Mahyar Mohtadi¹, Matthias Prange¹, Delia W. Oppo², Ricardo De Pol-Holz³, Ute Merkel¹, Xiao Zhang¹, Stephan Steinke¹ & Andreas Lückge⁴

The response of the tropical climate in the Indian Ocean realm to abrupt climate change events in the North Atlantic Ocean is contentious. Repositioning of the intertropical convergence zone is thought to have been responsible for changes in tropical hydroclimate during North Atlantic cold spells^{1–5}, but the dearth of high-resolution records outside the monsoon realm in the Indian Ocean precludes a full understanding of this remote relationship and its underlying mechanisms. Here we show that slowdowns of the Atlantic meridional overturning circulation during Heinrich stadials and the Younger Dryas stadial affected the tropical Indian Ocean hydroclimate through changes to the Hadley circulation including a southward shift in the rising branch (the intertropical convergence zone) and an overall weakening over the southern Indian Ocean. Our results are based on new, high-resolution sea surface temperature and seawater oxygen isotope records of well-dated sedimentary archives from the tropical eastern Indian Ocean for the past 45,000 years, combined with climate model simulations of Atlantic circulation slowdown under Marine Isotope Stages 2 and 3 boundary conditions. Similar conditions in the east and west of the basin rule out a zonal dipole structure as the dominant forcing of the tropical Indian Ocean hydroclimate of millennial-scale events. Results from our simulations and proxy data suggest dry conditions in the northern Indian Ocean realm and wet and warm conditions in the southern realm during North Atlantic cold spells.

In the North Atlantic, the most recent glacial and deglacial periods are characterized by a series of abrupt and severe cold snaps of millennial duration associated with either iceberg instabilities and surges (Heinrich events) or freshwater input from the Arctic Ocean⁶ (the Younger Dryas). These abrupt events are of particular interest because they were rapidly communicated through the ocean by a slowdown, or potentially a shut-down, of the Atlantic meridional overturning circulation⁷ (AMOC) and through the atmospheric circulation⁸ causing climate anomalies worldwide. Climate archives document a significant tropical hydrologic response to these events. Dry Younger Dryas and Heinrich stadials have been reported from various marine and terrestrial archives across the tropical Indian Ocean^{4,9–14}. However, a few records suggest wet Younger Dryas or Heinrich stadials over northeast Australia¹⁵, southern Indonesia^{5,16} and southeast Africa^{12,17}.

Although there seems to be strong evidence that the intertropical convergence zone (ITCZ) moved southwards in the tropical Atlantic², a wide range of mechanisms have been offered to explain the connection between the cooling of the North Atlantic and tropical Indian Ocean hydroclimates: a weakening of the rainfall system in response to regional sea surface cooling^{13,14}; and changes in the monsoon intensity^{4,10,16} associated with a southward shift in the mean¹ or winter^{4,5,15} position of the ITCZ or in the position of oceanic fronts¹⁸. However, there are no high-resolution records from the region of the tropical Indian Ocean unaffected by monsoon seasonality. Records from this region are needed to evaluate whether the eastern and western Indian Ocean experienced similar or contrasting rainfall anomalies during abrupt climate events. Furthermore, the Younger Dryas signal in many of the available records is ambiguous at best, and

almost none of them include data associated with North Atlantic millennial events older than Heinrich stadial 1.

The effect of AMOC slowing on tropical climate can be studied with freshwater hosing experiments using coupled atmosphere–ocean general circulation models. Such numerical experiments consistently show a southward displacement of the ITCZ over the Atlantic Ocean in response to North Atlantic cooling induced by a perturbation of the AMOC^{1,19,20}. However, these experiments provide ambiguous results

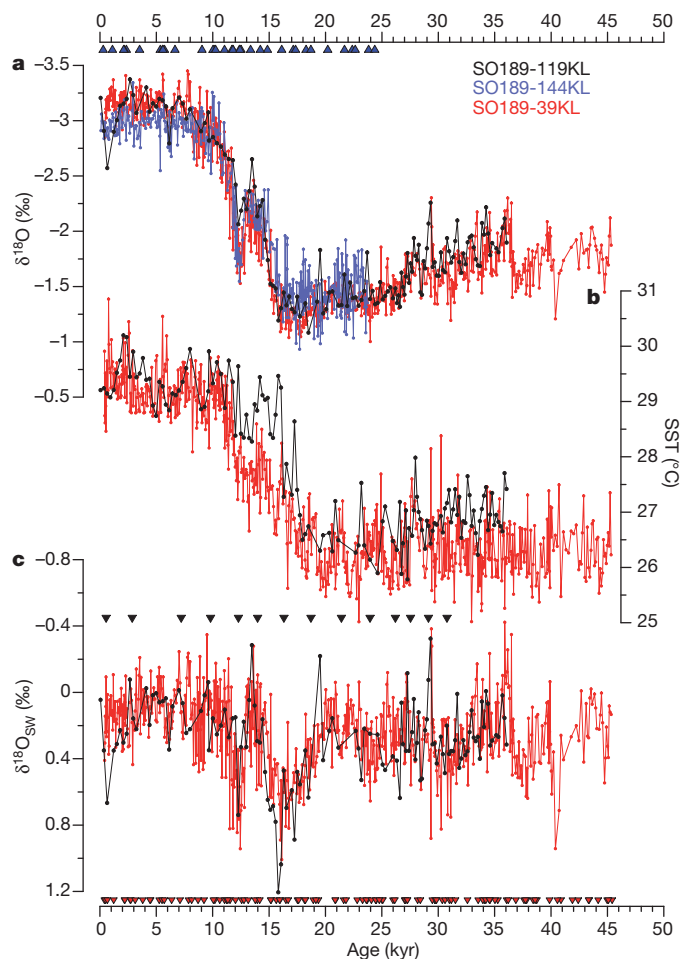


Figure 1 | Hydroclimate records from the eastern tropical Indian Ocean. Time series of $\delta^{18}\text{O} = (^{18}\text{O}/^{16}\text{O})_{\text{sample}} / (^{18}\text{O}/^{16}\text{O})_{\text{standard}} - 1$ (where the standard is Pee Dee Belemnite (PDB)) (a), SST (b) and $\delta^{18}\text{O}_{\text{SW}}$ (seawater $\delta^{18}\text{O}$ with standard mean ocean water as the standard) (c). The chronology of each core is established independently by ^{14}C accelerator mass spectrometry dating (triangles; see Methods). There is a large similarity between all records during the time they overlap, with no glacial–interglacial difference in the sea-level-corrected $\delta^{18}\text{O}_{\text{SW}}$.

¹MARUM-Center for Marine Environmental Sciences, University of Bremen, 28359 Bremen, Germany. ²Geology and Geophysics, Woods Hole Oceanographic Institution, Woods Hole, Massachusetts 02543, USA. ³Department of Oceanography, University of Concepción, Concepción, Chile. ⁴Federal Institute for Geosciences and Natural Resources, 30655 Hannover, Germany.

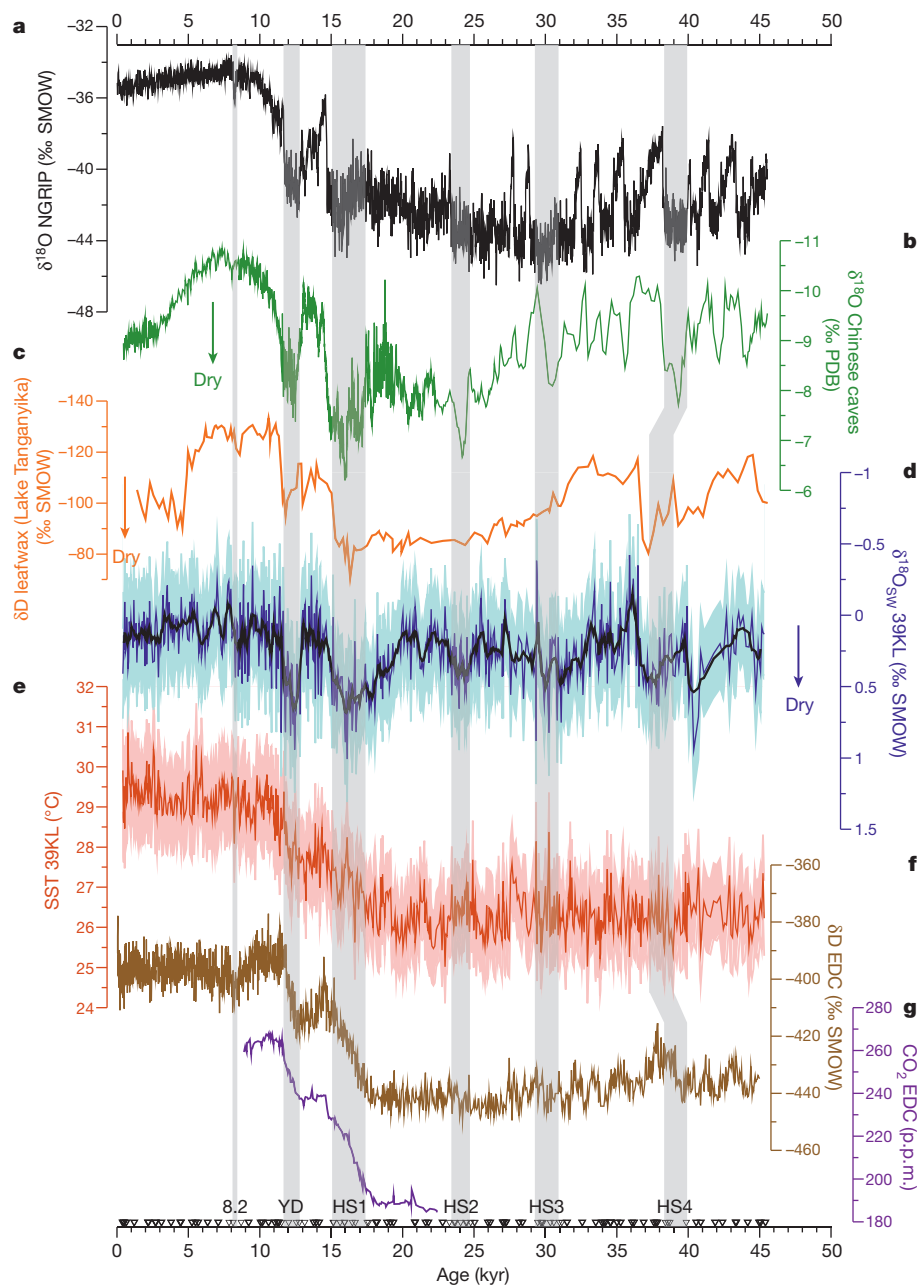


Figure 2 | Comparison of East Indian Ocean $\delta^{18}\text{O}_{\text{SW}}$ and SST data with other records of palaeoclimate. **a**, $\delta^{18}\text{O}$ data of Greenland ice core NGRIP²⁹; **b**, stack $\delta^{18}\text{O}$ record of Chinese speleothems³⁰; **c**, deuterium isotopes (δD) of leaf wax from Lake Tanganyika¹⁴; **d**, sea-level-corrected $\delta^{18}\text{O}_{\text{SW}}$ of core 39KL off western Sumatra (this study; black line represents a 7-point running average); **e**, SST reconstruction at site 39KL off western Sumatra (this study).

Envelopes in **d** and **e** indicate 1σ errors (Methods). **f**, δD data from the EPICA Dome C ice core²². **g**, Deglacial CO_2 record from the EPICA Dome C ice core²². Grey bars indicate the 8.2 kyr event, the Younger Dryas (YD), and Heinrich stadials (HSs) 1 to 4 as recorded in North Atlantic deep-sea cores²³. Triangles indicate the accelerator mass spectrometry ^{14}C age control points for core 39KL (this study).

for the tropical Indo-Pacific region, with the response and sensitivity of the region to North Atlantic freshwater perturbations being strongly model dependent²⁰. Thus, palaeoclimate data are invaluable for identifying mechanisms of hydrologic change outside the Atlantic realm.

Here we present three high-resolution marine sedimentary records from the western coast of Sumatra spanning the past 45 kyr. The age models for these cores are well constrained and are based on a total of 162 radiocarbon dates (Methods and Supplementary Table 1). We measured shell Mg/Ca ratios (806 samples) and stable oxygen isotopes ($\delta^{18}\text{O}$; 1,191 samples) of the surface-dwelling planktonic foraminifera *Globigerinoides ruber sensu stricto* to reconstruct variations in seawater $\delta^{18}\text{O}$ ($\delta^{18}\text{O}_{\text{SW}}$; Methods). These records include the first high-resolution paired Mg/Ca– $\delta^{18}\text{O}_{\text{SW}}$ record (average sampling time, 60 yr) from the equatorial eastern Indian

Ocean, which provides a measure of hydrological changes during the past 45 kyr (Fig. 1). Modern observations and instrumental records from the non-upwelling fore-arc basins off northern and central Sumatra, where our sites are located, suggest minor seasonal changes in precipitation, sea surface temperature (SST) and salinity compared with the upwelling region off south Java, and confirm that the study area lies outside the main Australasian monsoonal rainfall domains (Methods). Whereas records from other areas of the Indo-Pacific warm pool may be decoupled from local precipitation owing to oceanic advection²¹, salinity at our core sites is primarily driven by local rainfall and runoff (Methods). We therefore infer that the observed changes in our proxy records reflect local precipitation and can be used to unravel the response of the tropical eastern Indian Ocean during the Younger Dryas and Heinrich events.

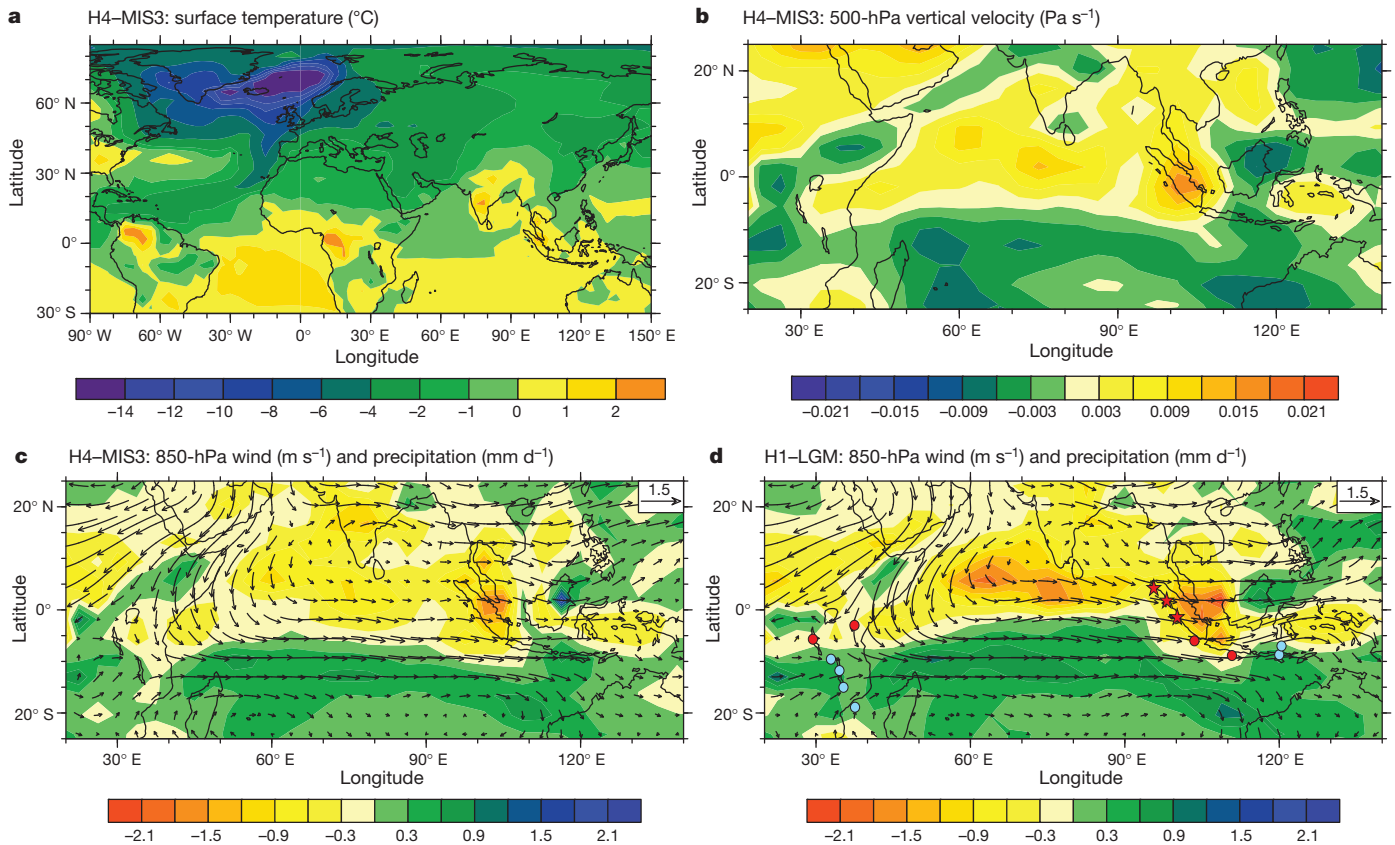


Figure 3 | Results from the CCSM3 simulations of Heinrich stadials 1 and 4. Plots show the difference between the Heinrich (hosing) experiments and the baseline simulations (MIS3 for H4 and LGM for H1; see Methods) as annual means. **a**, Surface temperature anomaly during H4, showing cooling over the Northern Hemisphere and warming in the Southern Hemisphere. **b**, Vertical velocity anomaly in the mid-level (500-hPa) atmosphere, with negative and positive values respectively indicating anomalously rising and sinking air during H4. The ascending branch of the annual mean Hadley circulation over the Indian

Ocean is displaced southwards. **c**, 850-hPa wind (arrows) and precipitation (shading) anomalies during H4. Westerly low-level wind anomalies are associated with wetter southern Indian Ocean and drier equatorial and northern Indian Ocean. **d**, Same as **c** but for the simulation of H1. Note the similarity between **c** and **d**, and the competing influence of the Pacific Walker cell on the eastern part of the maritime continent. Red stars (this study) and dots^{4,10,14,27} show sites indicating dry conditions during Heinrich stadial 1; blue dots show sites indicating wet Heinrich stadial 1 or Younger Dryas^{5,12,16,17}.

Reconstructed SST, $\delta^{18}\text{O}$ and $\delta^{18}\text{O}_{\text{SW}}$ from all sites show a remarkably consistent pattern during times when they overlap (Fig. 1), suggesting a coherent response from central to northern Sumatra. The SST records indicate that the deglacial warming of about 3°C started $18,300 \pm 330$ yr ago (1σ ; see Methods), synchronously (within dating uncertainties) with southern high-latitude climate change and an increase in atmospheric CO_2 concentration occurring during this period²² (Fig. 2).

Although the sea-level-corrected $\delta^{18}\text{O}_{\text{SW}}$ records show no glacial–interglacial change, the values increase during the Northern Hemisphere climate cold spells, as recorded in Greenland ice cores. Our records suggest decreased precipitation in the tropical eastern Indian Ocean that is most prominent during Heinrich stadials 1 and 4 and the Younger Dryas (Fig. 2). The difference between the age of Heinrich stadial 4 as defined in our marine records from off Sumatra and that derived from Greenland ice cores or Chinese speleothems (Fig. 2) is within the average 2σ error, which is larger than 2 kyr in sediment older than 35 kyr (Methods). Thus, on the basis of the similar timing of younger millennial events in our $\delta^{18}\text{O}_{\text{SW}}$ record and North Atlantic cold events, we argue that the high- $\delta^{18}\text{O}_{\text{SW}}$ interval near the documented age of Heinrich event 4 defined by layers containing peaks of ice-rafted detritus in North Atlantic marine records²³ is also synchronous with that event.

To elucidate the dynamics of changes in the tropical Indian Ocean hydroclimate forced by the North Atlantic, we performed and analysed freshwater hosing experiments under Marine Isotope Stages (MIS) 2 and 3 boundary conditions using the comprehensive coupled climate model CCSM3. More precisely, baseline simulations of the Last Glacial Maximum (LGM; 21 kyr ago (MIS2)) and the time slice from 38 kyr ago (MIS3)

were perturbed by 0.2 Sv ($1\text{ Sv} = 10^6\text{ m}^3\text{ s}^{-1}$) freshwater injections into the northern North Atlantic for 500 yr, mimicking Heinrich events 1 and 4 (Methods), two of the most pronounced events in our records. North Atlantic water hosing results in a drastic slowdown of the AMOC by $\sim 10\text{ Sv}$ in both glacial experiments (Methods) and, owing to the reduced northward Atlantic heat transport, a cooling of the surface of the North Atlantic (Fig. 3a). This cooling quickly propagates zonally throughout the Northern Hemisphere through atmospheric advection by the westerly winds and mixing¹⁹. The tropical mean circulation responds to the Northern Hemisphere cooling (and Southern Hemisphere warming) by generating anomalous energy transport from the southern hemisphere to the northern hemisphere. This energy transport is accomplished by a reorganization of the mean Hadley circulation involving an anomalous northward cross-equatorial flow in the upper branch accompanied by an anomalous southward flow in the lower branch²⁴. Over the southern Indian Ocean, this results in a weakening of the annual mean Hadley circulation involving a southward shift of its rising branch, reflected by a north–south dipole structure in the mid-tropospheric vertical velocity anomaly (Fig. 3b). The reorganization of the Hadley circulation is associated with a westerly, low-level wind anomaly over the equatorial and south equatorial Indian Ocean (Fig. 3c; northwesterly at the surface (not shown)). This weakening of the southeast trade winds that cross the Equator reduces upwelling in the Arabian Sea (where there are weaker southwesterly winds), as also suggested by proxy records from this region²⁵. Moreover, strengthening of the eastward winds over the Equator, a unique feature in the Indian Ocean responsible for warm equatorial waters, also contributes to the warming in the eastern tropical Indian Ocean.

The vertical velocity anomalies are associated with precipitation anomalies inducing drier conditions over the equatorial and north Indian Ocean and more humid conditions south of there (Fig. 3c). In particular, the model simulates a negative rainfall anomaly over Sumatra, whereas rainfall over southern Indonesia increases. The regional climatic response is qualitatively the same in both glacial hosing experiments (that is, under LGM and MIS3 boundary conditions), indicating that the same mechanisms may have been at work during all Heinrich stadials of the last glacial period (Fig. 3d and Methods). Despite the caveat of using a single model, the model results are consistent with our proxy data and also with Heinrich stadial 1 signals from other sites in the tropical Indian Ocean realm. Records suggesting humid conditions in Southern Indonesia and northern Australia during the Younger Dryas and Heinrich stadial 1^{5,15,16} lie within the easternmost part of the anomalous Indian Ocean Hadley cell, which is confined by the ascending branch of the Pacific Walker cell (Fig. 3). Likewise, lake records from East Africa that suggest humid conditions during Heinrich stadial 1^{12,17} lie beneath the ascending branch of the anomalous Hadley cell (Fig. 3). The remaining records of hydrological changes from the equatorial and northern Indian Ocean^{26,27} (including our records) suggest drier conditions during Heinrich stadial 1, in agreement with our model simulation. As part of the Hadley cell reorganization during Heinrich stadials, the Indian summer monsoon weakens. This weakening has been recently attributed to anomalous SST forcing in the tropical Atlantic that affects the Indian monsoon via a tropical atmospheric pathway³. Our model results suggest a rapid response of the Indian monsoon to North Atlantic abrupt events through both a stationary Rossby wave-train teleconnection that originates in the northern North Atlantic and a tropical atmospheric pathway (Methods).

Our results suggest that the North Atlantic climate cold spells affect the hydrology of the tropical Indian Ocean through a reorganization of the Hadley circulation including a southward displacement of the ITCZ. This finding suggests that northern Indian Ocean cooling alone cannot explain tropical Indian Ocean hydrology during the Younger Dryas and Heinrich stadials. Indeed, our SST reconstructions show a slight warming during several Heinrich stadials, suggesting that at least in central-northern Sumatra, reduced rainfall was not a response to local SST cooling. Comparison of our data from the eastern tropical Indian Ocean with the Lake Tanganyika humidity record from East Africa¹⁴ reveals a strong similarity ($r = 0.43$ with the range [0.11, 0.67], 95% confidence interval; Methods) with dry Younger Dryas and Heinrich stadials on both sides of the tropical Indian Ocean (Fig. 2), and suggests that zonally asymmetric changes within the Indian Ocean¹⁴ were not the main control on Indian Ocean hydrology during these periods. Our results suggest that decreases in the monsoon intensity²⁸ stem from a reorganization of the Hadley cell over the Indian Ocean realm (Fig. 3), with heterogeneous mean annual and seasonal SST anomalies over the tropical Indian Ocean (Methods).

Integrated palaeoclimate data and model results from this study reveal that drastic changes in the tropical Indian Ocean climate appear as a robust response to the AMOC slowdown during Heinrich stadials and the Younger Dryas. This response involves similar mechanisms regardless of glacial background climate states. These climatic changes involve a reorganization of the Hadley circulation, with a southward shift of the ITCZ across the entire equatorial Indian Ocean. The resulting precipitation anomaly mirrors the meridional dipole-shaped rainfall anomaly in the tropical Atlantic region². By contrast, our data suggesting little glacial–interglacial hydrologic change in the eastern Indian Ocean add to a growing body of evidence that the response of regional hydroclimate on millennial timescales was substantially greater than that on glacial–interglacial timescales^{21,26}.

METHODS SUMMARY

Piston cores SO189-119KL (3° 31' N, 96° 19' E; 780-cm core length, 808-m water depth), SO189-144KL (1° 9' N, 98° 4' E; 822-cm core length, 481-m water depth) and SO189-39KL (0° 47' S, 99° 54' E; 1,350-cm core length, 517-m water depth) were collected from the fore-arc basins off western Sumatra: the Simeulue basin (119KL), the Nias basin (144KL) and the northern Mentawai basin (39KL). Age models were

based on linear interpolation between a total of 162 radiocarbon dates (Supplementary Table 1 and Extended Data Fig. 4). For $\delta^{18}\text{O}$ analysis, the isotopic composition of the carbonate sample was measured using a Finnigan MAT 251 mass spectrometer on the CO_2 gas evolved by treatment with phosphoric acid at a constant temperature of 75 °C. The Mg/Ca cleaning protocol consisted of five water and two methanol washes, two oxidation steps with 1% NaOH-buffered H_2O_2 , and a weak acid leach with 0.001 M QD HNO_3 . Samples were then dissolved into 0.075 M QD HNO_3 and centrifuged for 10 min at 6,000 r.p.m., transferred into test tubes and diluted. Mg/Ca ratios were measured using a Perkin Elmer Optima 3300 R inductively coupled plasma optical emission spectrophotometer for samples from core 199KL, and an Agilent Technologies 700 Series inductively coupled plasma optical emission spectrophotometer for samples from core 39KL. For details, see Methods and Extended Data. For the numerical experiments, the comprehensive global climate model CCSM3 was used. The baseline simulations for LGM and MIS3 comprise the orbital parameters, greenhouse gas concentrations, sea level and continental ice sheets at, respectively, 21 and 38 kyr ago. For the Heinrich stadial 1 and 4 experiments, the LGM and, respectively, MIS3 climate states were perturbed by a constant freshwater input of 0.2 Sv to the northern North Atlantic. The hosing experiments were integrated for 500 yr. For each experiment, the mean of the past 100 simulation years was used for analysis. For details, see Methods and Extended Data.

Data reported here are stored in the Pangaea database (www.pangaea.de).

Online Content Any additional Methods, Extended Data display items and Source Data are available in the online version of the paper; references unique to these sections appear only in the online paper.

Received 25 August 2013; accepted 28 February 2014.

- Lewis, S. C. *et al.* High-resolution stalagmite reconstructions of Australian-Indonesian monsoon rainfall variability during Heinrich stadial 3 and Greenland interstadial 4. *Earth Planet. Sci. Lett.* **303**, 133–142 (2011).
- Arbuszewski, J. A., deMenocal, P. B., Cleroux, C., Bradtmiller, L. & Mix, A. Meridional shifts of the Atlantic intertropical convergence zone since the Last Glacial Maximum. *Nature Geosci.* **6**, 959–962 (2013).
- Marzin, C., Kallel, N., Kageyama, M., Duplessy, J.-C. & Braconnot, P. Glacial fluctuations of the Indian monsoon and their relationship with North Atlantic climate: new data and modelling experiments. *Clim. Past* **9**, 2135–2151 (2013).
- Mohtadi, M. *et al.* Glacial to Holocene swings of the Australian-Indonesian monsoon. *Nature Geosci.* **4**, 540–544 (2011).
- Muller, J., McManus, J. F., Oppo, D. W. & Francois, R. Strengthening of the Northeast Monsoon over the Flores Sea, Indonesia, at the time of Heinrich event 1. *Geology* **40**, 635–638 (2012).
- Condrin, A. & Winsor, P. Meltwater routing and the Younger Dryas. *Proc. Natl Acad. Sci. USA* **109**, 19928–19933 (2012).
- McManus, J. F., Francois, R., Gherardi, J. M., Keigwin, L. D. & Brown-Leger, S. Collapse and rapid resumption of Atlantic meridional circulation linked to deglacial climate changes. *Nature* **428**, 834–837 (2004).
- Moreno, P. I., Jacobson, G. L., Lowell, T. V. J. & Denton, G. H. Interhemispheric climate links revealed by a late-glacial cooling episode in southern Chile. *Nature* **409**, 804–808 (2001).
- Deplazes, G. *et al.* Links between tropical rainfall and North Atlantic climate during the last glacial period. *Nature Geosci.* **6**, 213–217 (2013).
- Mohtadi, M., Steinke, S., Lückge, A., Groenewald, J. & Hathorne, E. C. Glacial to Holocene surface hydrography of the tropical eastern Indian Ocean. *Earth Planet. Sci. Lett.* **292**, 89–97 (2010).
- Partin, J. W., Cobb, K. M., Adkins, J. F., Clark, B. & Fernandez, D. P. Millennial-scale trends in west Pacific warm pool hydrology since the Last Glacial Maximum. *Nature* **449**, 452–455 (2007).
- Thomas, D. S. G., Burrough, S. L. & Parker, A. G. Extreme events as drivers of early human behaviour in Africa? The case for variability, not catastrophic drought. *J. Quaternary Sci.* **27**, 7–12 (2012).
- Stager, J. C., Ryves, D. B., Chase, B. M. & Pausata, F. S. R. Catastrophic drought in the Afro-Asian monsoon region during Heinrich event 1. *Science* **331**, 1299–1302 (2011).
- Tierney, J. E. *et al.* Northern hemisphere controls on tropical southeast African Climate during the past 60,000 years. *Science* **322**, 252–255 (2008).
- Muller, J. *et al.* Possible evidence for wet Heinrich phases in tropical NE Australia: the Lynch's crater deposit. *Quat. Sci. Rev.* **27**, 463–475 (2008).
- Griffiths, M. L. *et al.* Increasing Australian-Indonesian monsoon rainfall linked to early Holocene sea-level rise. *Nature Geosci.* **2**, 636–639 (2009).
- Scheffé, E., Kuhlmann, H., Mollenhauer, G., Prange, M. & Pätzold, J. Forcing of wet phases in southeast Africa over the past 17,000 years. *Nature* **480**, 509–512 (2011).
- De Deckker, P., Moros, M., Perner, K. & Jansen, E. Influence of the tropics and southern westerlies on glacial interhemispheric asymmetry. *Nature Geosci.* **5**, 266–269 (2012).
- Clement, A. C. & Peterson, L. C. Mechanisms of abrupt climate change of the last glacial period. *Rev. Geophys.* **46**, RG4002 (2008).
- Kageyama, M. *et al.* Climatic impacts of fresh water hosing under Last Glacial Maximum conditions: a multi-model study. *Clim. Past* **9**, 935–953 (2013).
- Gibbons, F. T. *et al.* Deglacial $\delta^{18}\text{O}$ and hydrologic variability in the tropical Pacific and Indian Oceans. *Earth Planet. Sci. Lett.* **387**, 240–251 (2014).
- Parrenin, F. *et al.* Synchronous change of atmospheric CO_2 and Antarctic temperature during the Last Deglacial Warming. *Science* **339**, 1060–1063 (2013).

23. Hemming, S. R. Heinrich events: massive late Pleistocene detritus layers of the North Atlantic and their global climate imprint. *Rev. Geophys.* **42**, RG1005 (2004).
24. Frierson, D. M. W. *et al.* Contribution of ocean overturning circulation to tropical rainfall peak in the Northern Hemisphere. *Nature Geosci.* **6**, 940–944 (2013).
25. Pourmand, A., Marcantonio, F. & Schulz, H. Variations in productivity and eolian fluxes in the northeastern Arabian Sea during the past 110 ka. *Earth Planet. Sci. Lett.* **221**, 39–54 (2004).
26. Carolin, S. A. *et al.* Varied response of Western Pacific hydrology to climate forcings over the Last Glacial Period. *Science* **340**, 1564–1566 (2013).
27. Verschuren, D. *et al.* Half-precessional dynamics of monsoon rainfall near the East African Equator. *Nature* **462**, 637–641 (2009).
28. Tierney, J. E. & deMenocal, P. B. Abrupt shifts in Horn of Africa hydroclimate since the Last Glacial Maximum. *Science* **342**, 843–846 (2013).
29. Svensson, A. *et al.* A 60000 year Greenland stratigraphic ice core chronology. *Clim. Past* **4**, 47–57 (2008).
30. Wang, Y. *et al.* Millennial- and orbital-scale changes in the East Asian monsoon over the past 224,000 years. *Nature* **451**, 1090–1093 (2008).

Supplementary Information is available in the online version of the paper.

Acknowledgements We are grateful to K. Olafsdottir, M. Segl and B. Meyer-Schack for technical support. This study was funded by the German Bundesministerium für Bildung und Forschung (grant 03G0189A) and the Deutsche Forschungsgemeinschaft (DFG grants HE3412/15-1 and STE1044/4-1, and the DFG Research Centre/Cluster of Excellence 'The Ocean in the Earth System'). Climate model simulations were performed on the SGI Altix supercomputer of the Norddeutscher Verbund für Hoch- und Höchstleistungsrechnen. D.W.O. is funded by the US NSF, R.D.P.-H. is supported by Chilean FONDAP 15110009/ICM Nucleus NC120066.

Author Contributions M.M., D.W.O. and A.L. designed the study. M.P., U.M. and X.Z. designed, performed and analysed the climate model experiments. M.M. and S.S. generated and analysed the proxy data. R.D.P.-H., M.M. and D.W.O. were responsible for the radiocarbon analyses. M.M. and M.P. wrote the manuscript; all authors discussed the manuscript.

Author Information Reprints and permissions information is available at www.nature.com/reprints. The authors declare no competing financial interests. Readers are welcome to comment on the online version of the paper. Correspondence and requests for materials should be addressed to M.M. (mmohtadi@marum.de).

METHODS

Modern climate of the study area. At present the study area is characterized by only moderate monthly or seasonal changes in SST, air temperature, sea surface salinity (SSS) and precipitation (Extended Data Fig. 1). Mean annual SST averaged between 1854 and 2008 is about 29 °C with a small seasonal range of only 1.2 °C for the Simeulue basin, and 1.1 °C for the northern Mentawai and Nias basins (Extended Data Fig. 1, <http://nomads.ncdc.noaa.gov/las/getUI.do>). Likewise, 24-h air temperatures show little variability and are on average 26.7 °C with a small seasonal range of 2 °C near the core 119KL (station Sabang, averaged between 1976 and 1989; Extended Data Fig. 1) and one of 26.3 °C with a seasonal range of 0.9 °C near the core 39KL (station Padang, averaged between 1850 and 1989; <http://climexp.knmi.nl>; Extended Data Fig. 1). Generally, SST and air temperatures are highest during boreal spring because that is when near-surface winds are weakest, and are lowest during boreal fall owing to increased cloudiness and rainfall. Mean annual SSS is around 33.5 p.s.u. and varies seasonally within only ± 0.2 p.s.u. (ref. 31). Instrumental records of precipitation between 1879 and 1989 show higher average monthly rainfall over central-western Sumatra (~360 mm per month) compared with northwestern Sumatra (~135 mm per month) (<http://climexp.knmi.nl>; Extended Data Fig. 1). Although there are two precipitation maxima in the study area during spring and fall related to the seasonal migration of the ITCZ³², the contribution of each season to the total amount of rainfall does not vary considerably ($\sim 25\% \pm 5\%$; Extended Data Fig. 1).

These findings corroborate previous studies that exclude northern and western Sumatra from the Australasian monsoonal rainfall domains (see, for example, refs 32, 33). Observation and model studies suggest that there is no significant correlation between SST and rainfall variability in this region, between rainfall and ENSO³², or between SST and ENSO³⁴. In summary, the study area seems ideal to study the evolution of the hydrological changes in the tropical eastern Indian Ocean without significant biases introduced by variations in seasonal or interannual climate phenomena such as monsoon or ENSO.

The oceanic surface currents in the tropical eastern Indian Ocean flow according to the seasonally reversing monsoon winds. During boreal summer, a small branch of the northward flowing southwest monsoon current flows eastwards and joins the north equatorial counter current. This surface current is deflected southwards off the Sumatran coast and meets the south Java current off southwestern Sumatra (Extended Data Fig. 2). During summer, about 6 Sv of surface water flows southwards with the cross-equatorial meridional Ekman transport (MET), involving the export of low-salinity waters from the Bay of Bengal^{35–37}. During boreal winter, the direction of currents in the tropical eastern Indian Ocean is reversed (Extended Data Fig. 2). Westwards flowing surface waters join the northeast monsoon current south of Sri Lanka and are affected by the northwards-directed MET^{35,37}. Despite the seasonality in the currents, it seems that SST and SSS off northwestern Sumatra are not considerably affected by seasonally reversing surface current direction in the eastern Indian Ocean³⁷ or the strong salinity changes in the Bay of Bengal (see, for example, ref. 38; see also the next section).

Present and past control of $\delta^{18}\text{O}_{\text{SW}}$. The cores presented in this study have been collected close to the Sumatran coast that is separated from the open ocean by the Simeulue, Nias and Mentawai islands. During the last glacial period and Heinrich stadials, when sea level was up to 130 m lower than today, these fore-arc basins were more separated from the open ocean owing to their shallow sills of mostly <130 m (Extended Data Fig. 3). For the present, observation and model results suggest that “to the west of Sumatra, in particular, large rainfall and runoff persist year-round with enhanced surface stratification”³⁹ and that salinity off western Sumatra is strongly controlled by precipitation^{40–42}. Western Sumatra receives an annual freshwater flux of $\sim 1,800 \text{ mm yr}^{-1}$, where “a local maximum in P-E is present during all months, indicating that rainfall contributes to the existence of salinity stratified surface layer in this region”⁴². This overriding control of $\delta^{18}\text{O}_{\text{SW}}$ by local rainfall amount is also mirrored in our CTD data from two expeditions in 2005 and 2006 in this region: surface salinity at the core sites ranges between 32.5 p.s.u. (SO189-120MS at site 119KL and SO189-44MS at site 144KL) and 33 p.s.u. (SO189-40MS at site 39KL), whereas surface salinity west of the Mentawai Islands is as high as 34 p.s.u. (GeoB 10013-1 and 10018-1). This pattern supports previous findings that the low-salinity tongue off western Sumatra (and thus, $\delta^{18}\text{O}_{\text{SW}}$), particularly in the fore-arc basins of Mentawai, Nias and Simeulue, “is linked to the freshwater input in the near-surface layer from rainfall and river runoff”⁴³ rather than ocean advection. Sprintall *et al.*⁴⁴ and Janowiak and Xie⁴⁵ also stated that the freshwater pool located on the equator off the west Sumatra coast is related to a regional maximum in precipitation, as well as contribution from river runoff. We expect that these fore-arc basins were even more detached from large-scale surface circulation in the Indian Ocean during the last glacial period, when sea level was mostly below their sill depth.

In addition, a stalagmite record from Borneo²⁶ shows increased $\delta^{18}\text{O}$ values (of rainfall) during Heinrich stadials, in line with increased $\delta^{18}\text{O}_{\text{SW}}$ values in marine records from the Sulu Sea⁴⁶, the Lombok basin⁴⁷ and the Timor Sea⁴⁸ that lack any surface ocean connection to our study area. It is hard to explain such a consistent

pattern in terrestrial and marine archives without involving changes in regional convective activity.

Material and methods. Piston cores SO189-119KL (3° 31' N, 96° 19' E; 780-cm core length, 808-m water depth), SO189-144KL (1° 09' N, 98° 04' E; 822-cm core length, 481-m water depth) and SO189-39KL (0° 47' S, 99° 54' E; 1,350-cm core length, 517-m water depth) were collected from the upper continental margin in the Simeulue basin off northwestern Sumatra (119KL), from the Nias basin off northwestern Sumatra (144KL) and in the northern Mentawai basin off western Sumatra (39KL) during the RV *Sonne* cruise SO-189⁴⁹. The cores were sampled at 5-cm (119KL) and 2-cm (144KL, 39KL) steps. Core-top studies from the Simeulue basin, the Nias basin and the northern Mentawai basin suggest that these basins lack a calcite lysocline^{50,51}. The presence of well-preserved pteropods throughout the cores, along with the SEM observation of planktonic foraminifera in the corresponding core-tops, further supports the inference that selective calcite dissolution is, and has been, negligible at these sites.

Age models. The age model of SO189-119KL is based on 14 accelerator mass spectrometry (AMS) ¹⁴C dates and linear interpolation between them (Supplementary Table 1 and Extended Data Fig. 4). AMS ¹⁴C dating was performed on mixed planktonic foraminifera at the National Ocean Sciences Accelerator Mass Spectrometry Facility (NOSAMS) in Woods Hole, USA. The age model of SO189-39KL is based on linear interpolation between 112 AMS ¹⁴C dates performed on mixed planktonic foraminifera at NOSAMS (16 dates), on *Globigerinoides ruber* (41 dates), *Globigerinoides sacculifer* without the final sac-like chamber (45 dates), and on mixed *G. ruber* and *G. sacculifer* (10 dates) at the Keck Carbon Cycle Accelerator Mass Spectrometry Facility at the University of California in Irvine, USA (Supplementary Table 1 and Extended Data Fig. 4). The age model of SO189-144KL is based on linear interpolation between 36 AMS ¹⁴C dates performed on mixed planktonic foraminifera at NOSAMS (26 dates), on *G. ruber* (4 dates), on *G. sacculifer* without the final sac-like chamber (4 dates), on mixed *G. ruber* and *G. sacculifer* (1 date), and on mixed planktonic foraminifera (1 date) at the Keck Carbon Cycle Accelerator Mass Spectrometry Facility at the University of California in Irvine, USA (Supplementary Table 1 and Extended Data Fig. 4). All ages were corrected for ¹³C, and ¹⁴C ages were converted to calendar years using the CALIB 7.0-MARINE 13⁵² program without any local offset. This assumption is based on studies from the Andaman Islands⁵³ and the Nicobar Islands⁵⁴ showing insignificant deviations from the global reservoir effect (ΔR values of 11 yr and 17 yr, respectively) in this region.

The correlation between the AMS ¹⁴C dates in core 39KL shows statistically indistinguishable differences between the ages of monospecies and mixed species samples from the same core depths (Supplementary Fig. 1). We therefore included all the AMS ¹⁴C dates in the age model and calculated an average age for each depth. In core 144KL, mixed planktonic radiocarbon ages are on average about 200 yr older than the ages of the surface-dwelling species (*G. ruber* and *G. sacculifer*) during the Holocene, and about 500 yr older during the last deglaciation (Supplementary Table 1). These age offsets are most probably due to the basin topography, which is characterized by relatively shallow sills that hamper a rigorous exchange between the subsurface waters of the Nias basin and the open ocean today. Accordingly, a lower sea-level stand during the last deglaciation increased the residence time of subsurface waters and the age offset between pure surface and mixed surface–subsurface radiocarbon dates to 500 yr. Therefore, the mixed planktonic ages were corrected by 200 yr (Holocene) and 500 yr (last deglaciation), respectively. Additional control of the calculated age model for core 144KL is provided by its stable oxygen isotope ($\delta^{18}\text{O}$) record, which perfectly matches the $\delta^{18}\text{O}$ records of cores 39KL and 119KL (Fig. 1 and main text). According to the age models, the average sedimentation rate (SR) at 119KL is about 24 cm kyr⁻¹, with a higher average SR during MIS3 ($\sim 29 \text{ cm kyr}^{-1}$) than during the last deglaciation ($\sim 20 \text{ cm kyr}^{-1}$) and the Holocene ($\sim 19 \text{ cm kyr}^{-1}$). The average SR at 144KL is about 43 cm kyr⁻¹, with a higher average SR during the LGM ($\sim 51 \text{ cm kyr}^{-1}$) and the last deglaciation ($\sim 49 \text{ cm kyr}^{-1}$) than during the Holocene ($\sim 31 \text{ cm kyr}^{-1}$). The average SR at 39KL is about 34 cm kyr⁻¹, with no considerable differences between MIS3 ($\sim 32 \text{ cm kyr}^{-1}$), the last deglaciation ($\sim 34 \text{ cm kyr}^{-1}$) and the Holocene ($\sim 37 \text{ cm kyr}^{-1}$).

Stable oxygen isotope ($\delta^{18}\text{O}$), Mg/Ca and $\delta^{18}\text{O}_{\text{SW}}$. In total, 147 (651) samples for $\delta^{18}\text{O}$ and 135 (671) samples for Mg/Ca were analysed in core 119KL (39KL). Additional 393 samples were analysed for $\delta^{18}\text{O}$ in core 144KL. $\delta^{18}\text{O}$ and Mg/Ca analyses were performed on about 30 tests of *G. ruber sensu stricto*⁵⁵ from the 250–355- μm size fraction. Previous sediment trap⁵⁶ and sediment surface^{50,51} studies suggest that *G. ruber* tests record mean annual mixed-layer conditions in the tropical eastern Indian Ocean, and, in particular, mean annual surface conditions in the study area⁵¹.

For $\delta^{18}\text{O}$ analysis, the isotopic composition of the carbonate sample was measured using a Finnigan MAT 251 mass spectrometer on the CO₂ gas evolved by treatment with phosphoric acid at a constant temperature of 75 °C. For all stable isotope measurements, a working standard was used, which has been calibrated against VPDB (Vienna Pee Dee Belemnite) by using the NBS 19 standard. Long-term analytical

standard deviation is about $\pm 0.07\%$ (Isotope Laboratory at Faculty of Geosciences, University of Bremen).

For Mg/Ca analysis, samples were cleaned by applying a slight modification of the method originally proposed in ref. 57, consisting of five water washes and two methanol washes followed by two oxidation steps with 1% NaOH-buffered H_2O_2 and then a weak acid leach with 0.001 M QD HNO_3 . Samples were then dissolved into 0.075 M QD HNO_3 and centrifuged for 10 min at 6,000 r.p.m., transferred into test tubes and diluted. Mg/Ca ratios were measured using a Perkin Elmer Optima 3300 R inductively coupled plasma optical emission spectrophotometer (ICP-OES) equipped with an autosampler and a U-5000 AT ultrasonic nebulizer (Cetac Technologies) for samples from core 199KL, or an Agilent Technologies 700 Series ICP-OES with a CETAX ASX-520 autosampler for samples from core 39KL (both housed at the Faculty of Geosciences, University of Bremen). Mg/Ca values are reported as mmol mol^{-1} . The instrumental precision was determined using an external, in-house standard (Mg/Ca = 2.92 mmol mol^{-1}), which was run after every fifth sample. In core SO189-119KL, the relative standard deviations were 0.008 mmol mol^{-1} (0.26%) for the external standard and 0.07 mmol mol^{-1} (1.94%) for the ECRM 752-1 standard⁵⁸. Replicate measurements on 30 samples revealed an average standard deviation of 0.15 mmol mol^{-1} . In core SO189-39KL, the relative standard deviations were 0.005 mmol mol^{-1} (0.16%) for the external standard and 0.06 mmol mol^{-1} (1.66%) for the ECRM 752-1 standard. Replicate measurements on 55 samples revealed an average standard deviation of 0.12 mmol mol^{-1} . Clay contamination and post-depositional Mn-rich carbonate/oxyhydroxide coatings could be excluded by measuring Fe/Ca, Mn/Ca and Al/Ca ratios ($< 0.1 \text{ mmol mol}^{-1}$ for Mn/Ca and Fe/Ca; not detectable for Al/Ca). Mg/Ca ratios were converted to temperature following⁵⁹

$$\text{Mg/Ca} [\text{mmol mol}^{-1}] = 0.38e^{0.09T [^\circ\text{C}]} \quad (1)$$

To calculate $\delta^{18}\text{O}_{\text{SW}}$ as a measure of hydrologic changes, we used the following $\delta^{18}\text{O}$:temperature equation⁶⁰:

$$T [^\circ\text{C}] = 14.9 - 4.8(\delta^{18}\text{O}_{\text{cc}} - \delta^{18}\text{O}_{\text{SW}}) \quad (2)$$

where $\delta^{18}\text{O}_{\text{cc}}$ is the measured $\delta^{18}\text{O}$ of calcite and T is the Mg/Ca-derived temperature. The values were then converted to standard mean ocean water (SMOW) by adding 0.27‰ and corrected for sea-level changes proposed in ref. 61.

Error analysis for SST and $\delta^{18}\text{O}_{\text{SW}}$. The errors in $\delta^{18}\text{O}_{\text{SW}}$ and SST reconstructions are estimated by propagating the error introduced by the $\delta^{18}\text{O}_{\text{cc}}$ and Mg/Ca measurements (see previous section), the Mg/Ca:temperature calibration (equation (1)), the $\delta^{18}\text{O}$:temperature equation (equation (2)) and the removal of the global ice volume⁶¹ ($\pm 0.09\%$). For the SST estimate, the following equation was used to propagate the errors by assuming no covariance among the errors⁶²:

$$\sigma_T^2 = \left(\frac{\partial T}{\partial a} \sigma_a\right)^2 + \left(\frac{\partial T}{\partial b} \sigma_b\right)^2 + \left(\frac{\partial T}{\partial \text{Mg/Ca}} \sigma_{\text{Mg/Ca}}\right)^2$$

where

$$a = 0.090 \pm 0.003 \text{ } ^\circ\text{C}^{-1}$$

$$b = 0.38 \pm 0.02 \text{ mmol mol}^{-1}$$

$$\frac{\partial T}{\partial a} = -\frac{1}{a^2} \ln\left(\frac{\text{Mg/Ca}}{b}\right)$$

$$\frac{\partial T}{\partial b} = -\frac{1}{ab}$$

and

$$\frac{\partial T}{\partial \text{Mg/Ca}} = \frac{1}{a} \frac{1}{\text{Mg/Ca}}$$

For the $\delta^{18}\text{O}_{\text{SW}}$ estimate, the following equation was used to propagate the errors by assuming no covariance among the errors⁶²:

$$\sigma_{\delta^{18}\text{O}_{\text{SW}}}^2 = \left(\frac{\partial \delta^{18}\text{O}_{\text{SW}}}{\partial T} \sigma_T\right)^2 + \left(\frac{\partial \delta^{18}\text{O}_{\text{SW}}}{\partial a} \sigma_a\right)^2 + \left(\frac{\partial \delta^{18}\text{O}_{\text{SW}}}{\partial b} \sigma_b\right)^2 + \left(\frac{\partial \delta^{18}\text{O}_{\text{SW}}}{\partial \delta^{18}\text{O}_{\text{cc}}} \sigma_{\delta^{18}\text{O}_{\text{cc}}}\right)^2$$

where

$$a = 14.9 \pm 0.1 \text{ } ^\circ\text{C}$$

$$b = -4.8 \pm 0.08 \text{ } ^\circ\text{C}$$

$$\frac{\partial \delta^{18}\text{O}_{\text{SW}}}{\partial T} = -\frac{1}{b}$$

$$\frac{\partial \delta^{18}\text{O}_{\text{SW}}}{\partial a} = \frac{1}{b}$$

$$\frac{\partial \delta^{18}\text{O}_{\text{SW}}}{\partial b} = \frac{T}{b^2} - \frac{a}{b^2}$$

and

$$\frac{\partial \delta^{18}\text{O}_{\text{SW}}}{\partial \delta^{18}\text{O}_{\text{cc}}} = 1$$

The resulting errors are on average about 1 °C for SST and 0.3‰ for $\delta^{18}\text{O}_{\text{SW}}$ in cores 39KL and 119KL (Extended Data Fig. 5, Fig. 2 and main text). We note that the absolute SST values in 119KL are about 1 °C higher than in 39KL during the last deglaciation (Fig. 1 and main text). This difference is probably related to the more open Simeulue basin (site 119KL; see Extended Data Fig. 3). However, the calculated $\delta^{18}\text{O}_{\text{SW}}$ values for cores 119KL and 39KL are very similar, suggesting little influence of SST on $\delta^{18}\text{O}_{\text{SW}}$ and that the latter is mainly controlled by precipitation changes.

Estimating the timing of deglacial warming. To estimate the timing of deglacial warming from the Mg/Ca record of core 39KL, we applied a ramp-fitting method using RAMPFIT version 1.10 (<http://www.manfredmudelsee.com/soft/rampfit>)⁶³. RAMPFIT has successfully been applied in previous studies for change-point detection in palaeoclimatic time series^{64–67}. The simple ramp-function (three-phase) regression model assumes the existence of two distinct climate states, each of which is characterized by a constant parameter (here given by the SSTs of the cold glacial and the warm Holocene state), and a linear transition from one state to the other. Superimposed on this ramp function are short-term climate variations and noise from measurement uncertainties making visual determination of the two break points (that is, the start and end of the transition) difficult. RAMPFIT uses weighted least-squares regression to determine the amplitude of the transition, and a brute-force search (that is, a method that consists of systematically enumerating all possible candidates for the solution) for detecting start and end points. The time-dependent standard deviation provides the weights for the least-squares regression. Non-parametric stationary bootstrap re-sampling was used to estimate uncertainties in the timing of the transition, and age model uncertainties were not taken into account⁶³.

Because the SST time series of core 39KL shows a warming trend during the mid-to-late Holocene, data younger than 5 kyr were excluded from the ramp regression analysis. Taking the entire glacial period (that is, up to 45 kyr ago, the end of the SST record) into account, RAMPFIT estimates the onset of deglacial warming at 18.30 ± 0.33 kyr ago (1σ). This value is robust against the chosen interval length; for example, excluding MIS3 (that is, data older than 29 kyr) from the regression analysis leads to an estimated onset of deglacial warming at 18.29 ± 0.44 kyr ago (Extended Data Fig. 6). The break points between the deglacial transition and the early Holocene warm state were found to occur 9.62 ± 0.33 kyr ago and 9.75 ± 0.39 kyr ago for the 5–45-kyr and 5–29-kyr intervals, respectively (Extended Data Fig. 6). Mean Mg/Ca SSTs before and after the deglacial transition are 26.29 ± 0.03 and 29.18 ± 0.06 °C, respectively, when using the 5–45-kyr interval, and are 26.27 ± 0.06 and 29.16 ± 0.07 °C when using the 5–29 kyr interval.

Ramp-function regression has not been applied to the Mg/Ca record of core 119KL because its temporal resolution is too coarse. However, visual inspection suggests that deglacial warming started ~ 18 kyr ago, that is, synchronous with changes in atmospheric CO_2 and high-latitude temperature estimated from Antarctic ice cores²².

Correlation between $\delta^{18}\text{O}_{\text{SW}}$ in 39KL and δD in Lake Tanganyika. The correlation between the $\delta^{18}\text{O}_{\text{SW}}$ record of SO189-39KL and the δD record of Lake Tanganyika¹⁴ (Fig. 2 and main text) was tested by using the improved version of PEARSONT⁶⁸ (<http://www.manfredmudelsee.com/soft/pearson/index.htm>). The software estimates the correlation coefficient (r) with accurate bootstrap confidence intervals by accounting for the autocorrelation (memory) of the data⁶⁸. The two data sets were re-sampled at 0.3-kyr steps on the basis of their original age models to achieve the same timescale. The correlation coefficient and 95% confidence interval for the period 1.5–45 kyr ago is $r = 0.43 [0.11, 0.67]$. Because the confidence interval does not contain zero, the correlation between the two records is significant.

Numerical experiments. For the numerical experiments, the comprehensive global climate model CCSM3 (Community Climate System Model version 3, National Center for Atmospheric Research) was used. CCSM3 is a state-of-the-art, fully coupled model, composed of four separate components representing atmosphere, ocean, land and sea ice⁶⁹. In our simulations, the resolution of the atmospheric component is 3.75° with 26 layers in the vertical, and the ocean has a nominal resolution of 3° with

equatorial grid refinement in the meridional direction (down to 0.9°) and 25 levels in the vertical⁷⁰. The land model is defined on the same horizontal grid as the atmosphere and includes components for biogeophysics, biogeochemistry and the hydrologic cycle, as well as a dynamic global vegetation model^{71,72}. To improve the simulation of the land surface hydrology and vegetation cover, new parameterizations for canopy interception and soil evaporation have been implemented into the land component⁷³. Our experimental framework comprises four glacial simulations.

(1) A baseline simulation for the LGM following the guidelines of the Paleoclimate Modelling Intercomparison Project, Phase 2⁷⁴. The boundary conditions for this simulation comprise the orbital parameters⁷⁵ and the greenhouse gas concentrations of CO₂, CH₄ and N₂O (185 p.p.m., 350 p.p.b. and 200 p.p.b., respectively) from 21 kyr ago. A sea-level lowering by 120 m has been taken into account by modifying the land–sea distribution, which, in particular, leads to closure of the Bering Strait. In addition, LGM continental ice sheets have been implemented on the basis of the ICE-5G data set⁷⁶. The experimental set-up differs from the LGM run in ref. 77 only in the land surface component (see above). Our LGM simulation was integrated for 1,500 yr, starting from the quasi-equilibrated LGM run of ref. 77.

(2) A Heinrich stadial 1 analogue experiment in which the LGM climate state is perturbed by a constant freshwater input of 0.2 Sv to the northern North Atlantic, leading to a substantial weakening of the AMOC. The hosing experiment was integrated for 500 yr. Note that the applied freshwater forcing is in the range of published estimates for meltwater input during Heinrich events²³.

(3) A MIS3 baseline simulation in which the LGM boundary conditions (see above) were modified by applying the orbital forcing of 38 kyr ago and the corresponding greenhouse gas concentrations of CO₂, CH₄ and N₂O (215 p.p.m., 501 p.p.b. and 234 p.p.b., respectively; refs 78–80). In addition, the 38-kyr-ago ICE-5G continental ice-sheet distribution was implemented⁷⁶. The MIS3 baseline simulation was initialized with the final state of our LGM simulation and integrated for another 2,100 yr.

(4) A Heinrich stadial 4 simulation in which the MIS3 (38 kyr ago) baseline climate is perturbed by a constant 0.2-Sv freshwater influx analogous to that in the Heinrich stadial 1 experiment. The Heinrich stadial 4 hosing experiment started at year 1,600 of our MIS3 baseline run and was integrated for 500 yr.

In all simulations, ozone and aerosol distributions were kept at pre-industrial levels⁸¹. For each experiment, the mean of the last 100 simulation years was used for analysis.

Extended Data Fig. 7 shows the Atlantic meridional overturning stream functions for the four different glacial climate states along with a pre-industrial reference run. The LGM North Atlantic overturning is slightly (1–2 Sv) stronger than the pre-industrial circulation, but the southward flow of North Atlantic Deep Water takes place at shallower depth. The AMOC is similarly strong in the MIS3 baseline run. On freshwater input to the North Atlantic, the AMOC weakens rapidly under both LGM and MIS3 boundary conditions.

Extended Data Fig. 8 shows the annual mean climatic response to AMOC slowdown under LGM boundary conditions (Heinrich stadial 1 experiment) for large-scale surface temperature and mid-tropospheric vertical velocity in the Indian Ocean region. Comparing the results of the Heinrich stadial 1 experiment with the Heinrich stadial 4 run (Fig. 3 and main text) suggests that the same mechanisms are at work, involving a southward shift of the ascending branch of the annual mean Hadley circulation. For the same region, the mid-tropospheric vertical velocity is shown in Supplementary Fig. 2 for both the LGM and MIS3 baseline simulations as a reference. Rising air over the equatorial region with subsidence to the north and south reveals the regional annual mean Hadley circulation in both climate states.

Indian summer monsoon weakening and atmospheric Atlantic Ocean/India teleconnection. As part of the Hadley cell reorganization during Heinrich stadials, the Indian summer monsoon weakens (Extended Data Fig. 9). The model results suggest a rapid response of the Indian monsoon to North Atlantic cooling through both a stationary Rossby wave train teleconnection that originates in the northern North Atlantic and a tropical atmospheric pathway.

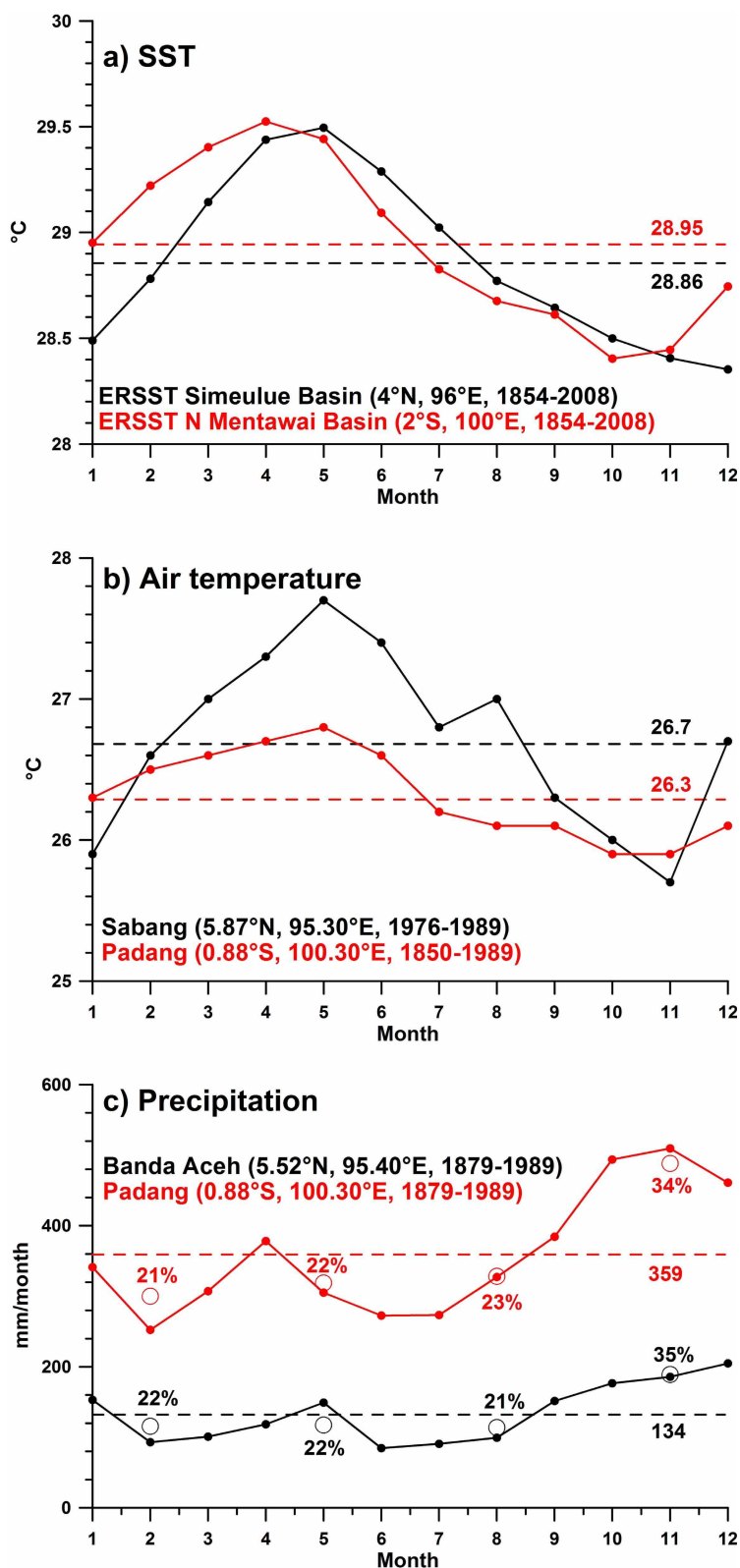
The 200-hPa wind field anomaly (Heinrich stadial 4 hosing experiment minus MIS3 baseline run) in summer exhibits an arch-shaped wave train that propagates southeastwards from the northern North Atlantic region of perturbation to west-central Asia via east-central Europe, and farther, zonally across Asia towards the Pacific Ocean along the westerly jet (Extended Data Fig. 10). Except north and northwest of India, this wave train has an equivalent barotropic structure (not shown). From analysing modern observational data, a similar wave train has been identified as part of a circumglobal teleconnection pattern in the summertime mid-latitude circulation of the Northern Hemisphere, which significantly correlates with Indian monsoonal rainfall at the interannual timescale⁸². It has been suggested that the upper-level circulation anomaly affects Indian rainfall by changing the intensity of the monsoonal easterly vertical shear and, hence, the monsoon dynamics^{82,83} (and moist dynamic instability). A westerly flow anomaly that stretches from North Africa to western India via the Arabian Sea adds to the upper-level circulation anomaly in the Indian monsoon region (Extended Data Fig. 10). A similar circulation anomaly over Africa and the

Arabian Sea was recently found in freshwater hosing experiments³ and, by means of atmosphere-only sensitivity experiments, could be attributed to anomalous SST forcing in the tropical Atlantic ('tropical pathway').

Unrelated to the Indian summer monsoon, an equivalent barotropic wave train propagating southeastwards from the northern North Atlantic source region is also found in the Heinrich stadial winter circulation anomaly (Extended Data Fig. 10). Compared with the summer season, the wave path is shifted towards the Equator following the seasonal jet stream displacement, crossing the Mediterranean Sea and the Arabian Peninsula until it reaches India, where an anticyclonic circulation anomaly develops in the upper troposphere. We surmise that this anomalous anticyclone promotes the upper-level southeasterly cross-equatorial flow over the Indian Ocean (Extended Data Fig. 10), which contributes to anomalous energy transport from the Southern Hemisphere to the anomalously cold Northern Hemisphere (compare with refs 24, 84). The increased energy demand of the Northern Hemisphere during Heinrich stadials is particularly large in the boreal winter season, when the Northern Hemisphere cooling is strongest (Supplementary Fig. 3), mainly owing to sea-ice effects (increased surface albedo and reduced ocean–atmosphere heat flux in the northern North Atlantic). We note that atmospheric circulation and precipitation response patterns are qualitatively the same in the Heinrich stadial 1 and Heinrich stadial 4 experiments (not shown).

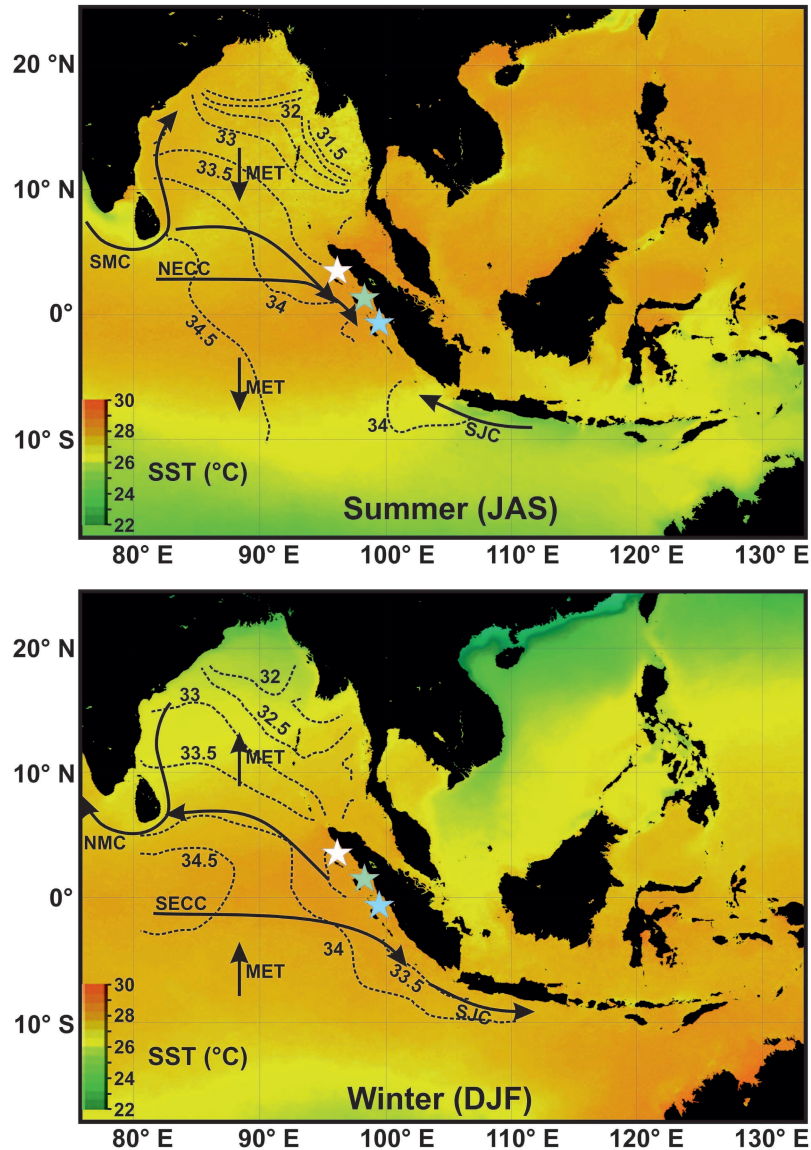
- Antonov, J. I., Locarnini, R. A., Boyer, T. P., Mishonov, A. V. & Garcia, H. E. *World Ocean Atlas 2005 Volume 2: Salinity* 182 (US Government Printing Office, 2006).
- Aldrian, E. & Susanto, R. D. Identification of three dominant rainfall regions within Indonesia and their relationship to sea surface temperature. *Int. J. Climatol.* **23**, 1435–1452 (2003).
- Wang, B. & Ding, Q. Global monsoon: dominant mode of annual variation in the tropics. *Dyn. Atmos. Oceans* **44**, 165–183 (2008).
- Yoo, S.-H., Yang, S. & Ho, C.-H. Variability of the Indian Ocean sea surface temperature and its impacts on Asian-Australian monsoon climate. *J. Geophys. Res.* **111**, D03108 (2006).
- Schott, F. A. & McCreary, J. P. The monsoon circulation of the Indian Ocean. *Prog. Oceanogr.* **51**, 1–123 (2001).
- Sengupta, D., Raj, G. N. B. & Shenoi, S. S. C. Surface freshwater from Bay of Bengal runoff and Indonesian Throughflow in the tropical Indian Ocean. *Geophys. Res. Lett.* **33**, L22609 (2006).
- Schott, F. A., Xie, S.-P. & McCreary, J. P. Jr. Indian Ocean circulation and climate variability. *Rev. Geophys.* **47**, RG1002 (2009).
- Vinayachandran, P. N., Murty, V. S. N. & Ramesh Babu, V. Observations of barrier layer formation in the Bay of Bengal during summer monsoon. *J. Geophys. Res.* **107**, 8018 (2002).
- Qu, T., Du, Y., Strachan, J., Meyers, G. & Slingo, J. M. Sea surface temperature and its variability in the Indonesian region. *Oceanography* **18**, 50–61 (2005).
- Du, Y., Qu, T., Meyers, G., Masumoto, Y. & Sasaki, H. Seasonal heat budget in the mixed layer of the southeastern tropical Indian Ocean in a high-resolution ocean general circulation model. *J. Geophys. Res.* **110**, C04012 (2005).
- Qu, T. & Meyers, G. Seasonal variation of barrier layer in the southeastern tropical Indian Ocean. *J. Geophys. Res.* **110**, C11003 (2005).
- Sprintall, J. & Tomczak, M. Evidence of the barrier layer in the surface layer of the tropics. *J. Geophys. Res.* **97**, 7305–7316 (1992).
- Qiu, Y., Cai, W., Li, L. & Guo, X. Argo profiles variability of barrier layer in the tropical Indian Ocean and its relationship with the Indian Ocean Dipole. *Geophys. Res. Lett.* **39**, L08605 (2012).
- Sprintall, J., Potemra, J. T., Hautala, S. L., Bray, N. A. & Pandoe, W. W. Temperature and salinity variability in the exit passages of the Indonesian Throughflow. *Deep Sea Res. Part II Top. Stud. Oceanogr.* **50**, 2183–2204 (2003).
- Janowiak, J. E. & Xie, P. CAMS-OP1: a global satellite rain gauge merged product for real-time precipitation monitoring applications. *J. Clim.* **12**, 3335–3342 (1999).
- Rosenthal, Y., Oppo, D. W. & Linsley, B. K. The amplitude and phasing of climate change during the last deglaciation in the Sulu Sea, western equatorial Pacific. *Geophys. Res. Lett.* **30**, 1428 (2003).
- Levi, C. et al. Low-latitude hydrological cycle and rapid climate changes during the last deglaciation. *Geochem. Geophys. Geosyst.* **8**, Q05N12 (2007).
- Zuraida, R. et al. Evidence for Indonesian Throughflow slowdown during Heinrich events 3–5. *Paleoceanography* **24**, PA2205 (2009).
- Wiedicke-Hombach, M. et al. *SUMATRA - The Hydrocarbon System of the Sumatra Forearc*. Vol. Archive No. 0126492 (Federal Institute for Geosciences and Natural Resources Hannover, 2007).
- Mohtadi, M. et al. Modern environmental conditions recorded in surface sediment samples off W and SW Indonesia: planktonic foraminifera and biogenic compounds analyses. *Mar. Micropaleontol.* **65**, 96–112 (2007).
- Mohtadi, M. et al. Reconstructing the thermal structure of the upper ocean: Insights from planktic foraminifera shell chemistry and alkenones in modern sediments of the tropical eastern Indian Ocean. *Paleoceanography* **26**, PA3219 (2011).
- Reimer, P. J. et al. IntCal13 and Marine13 radiocarbon age calibration curves 0–50,000 years cal BP. *Radiocarbon* **55**, 1869–1887 (2013).
- Dutta, K., Bhushan, K. & Somayajulu, B. L. K. ΔR correction values for the northern Indian Ocean. *Radiocarbon* **43**, 483–488 (2001).
- Southon, J., Kashgarian, M., Fontugne, M., Metivier, B. & Yim, W. W.-S. Marine reservoir corrections for the Indian Ocean and southeast Asia. *Radiocarbon* **44**, 167–180 (2002).

55. Wang, L. Isotopic signals in two morphotypes of *Globigerinoides ruber* (white) from the South China Sea: implications for monsoon climate change during the last glacial cycle. *Palaeogeogr. Palaeoclimatol. Palaeoecol.* **161**, 381–394 (2000).
56. Mohtadi, M. *et al.* Low-latitude control on seasonal and interannual changes in planktonic foraminiferal flux and shell geochemistry off south Java: a sediment trap study. *Paleoceanography* **24**, PA1201 (2009).
57. Barker, S., Greaves, M. & Elderfield, H. A study of cleaning procedures used for foraminiferal Mg/Ca paleothermometry. *Geochem. Geophys. Geosyst.* **4**, 8407 (2003).
58. Greaves, M. *et al.* Interlaboratory comparison study of calibration standards for foraminiferal Mg/Ca thermometry. *Geochem. Geophys. Geosyst.* **9**, Q08010 (2008).
59. Anand, P., Elderfield, H. & Conte, M. H. Calibration of Mg/Ca thermometry in planktonic foraminifera from a sediment trap time series. *Paleoceanography* **18**, 1050 (2003).
60. Bemis, B. E., Spero, H. J., Bijma, J. & Lea, D. W. Reevaluation of the oxygen isotopic composition of planktonic foraminifera: experimental results and revised paleotemperature equations. *Paleoceanography* **13**, 150–160 (1998).
61. Waelbroeck, C. *et al.* Sea-level and deep water temperature changes derived from benthic foraminifera isotopic records. *Quat. Sci. Rev.* **21**, 295–305 (2002).
62. Bevington, P. R. & Robinson, D. K. *Data Reduction and Error Analysis for the Physical Sciences* 3rd edn, 320 (McGraw-Hill, 2003).
63. Mudelsee, M. Ramp function regression: a tool for quantifying climate transitions. *Comput. Geosci.* **26**, 293–307 (2000).
64. Fleitmann, D. *et al.* Holocene forcing of the Indian monsoon recorded in a stalagmite from Southern Oman. *Science* **300**, 1737–1739 (2003).
65. Fleitmann, D. *et al.* Timing and climatic impact of Greenland interstadials recorded in stalagmites from northern Turkey. *Geophys. Res. Lett.* **36**, L19707 (2009).
66. Steffensen, J. P. *et al.* High-resolution Greenland ice core data show abrupt climate change happens in few years. *Science* **321**, 680–684 (2008).
67. Mudelsee, M. & Raymo, M. E. Slow dynamics of the Northern Hemisphere glaciation. *Paleoceanography* **20**, PA4022 (2005).
68. Mudelsee, M. Estimating Pearson's correlation coefficient with bootstrap confidence interval from serially dependent time series. *Math. Geol.* **35**, 651–665 (2003).
69. Collins, W. D. *et al.* The Community Climate System Model version 3 (CCSM3). *J. Clim.* **19**, 2122–2143 (2006).
70. Yeager, S. G., Shields, C. A., Large, W. G. & Hack, J. J. The low-resolution CCSM3. *J. Clim.* **19**, 2545–2566 (2006).
71. Levis, S., Bonan, G. B., Vertenstein, M. & Oleson, K. W. *The Community Land Model's Dynamic Global Vegetation Model (CLM-DGVM): Technical Description and User's Guide* (National Center for Atmospheric Research, 2004).
72. Oleson, K. *et al.* *Technical Description of the Community Land Model (CLM)*. (National Center for Atmospheric Research, 2004).
73. Oleson, K. W. *et al.* Improvements to the Community Land Model and their impact on the hydrological cycle. *J. Geophys. Res.* **113**, G01021 (2008).
74. Braconnot, P. *et al.* Results of PMIP2 coupled simulations of the Mid-Holocene and Last Glacial Maximum – Part 1: experiments and large-scale features. *Clim. Past* **3**, 261–277 (2007).
75. Berger, A. L. Long-term variations of daily insolation and Quaternary climate changes. *J. Atmos. Sci.* **35**, 2362–2367 (1978).
76. Peltier, W. R. Global glacial isostasy and the surface of the ice-age Earth: the ICE-5G (VM2) model and GRACE. *Annu. Rev. Earth Planet. Sci.* **32**, 111–149 (2004).
77. Merkel, U., Prange, M. & Schulz, M. ENSO variability and teleconnections during glacial climates. *Quat. Sci. Rev.* **29**, 86–100 (2010).
78. Flückiger, J. *et al.* N₂O and CH₄ variations during the last glacial epoch: insight into global processes. *Glob. Biogeochem. Cycles* **18**, GB1020 (2004).
79. Spahni, R. *et al.* Atmospheric methane and nitrous oxide of the Late Pleistocene from Antarctic ice cores. *Science* **310**, 1317–1321 (2005).
80. Ahn, J. & Brook, E. J. Atmospheric CO₂ and climate from 65 to 30 ka B.P. *Geophys. Res. Lett.* **34**, L10703 (2007).
81. Otto-Bliesner, B. L. *et al.* Climate sensitivity of moderate- and low-resolution versions of CCSM3 to preindustrial forcings. *J. Clim.* **19**, 2567–2583 (2006).
82. Ding, Q. & Wang, B. Circumglobal teleconnection in the Northern Hemisphere summer. *J. Clim.* **18**, 3483–3505 (2005).
83. Ding, Q. & Wang, B. Intraseasonal teleconnection between the summer Eurasian wave train and the Indian Monsoon. *J. Clim.* **20**, 3751–3767 (2007).
84. Broccoli, A. J., Dahl, K. A. & Stouffer, R. J. Response of the ITCZ to Northern Hemisphere cooling. *Geophys. Res. Lett.* **33**, L01702 (2006).



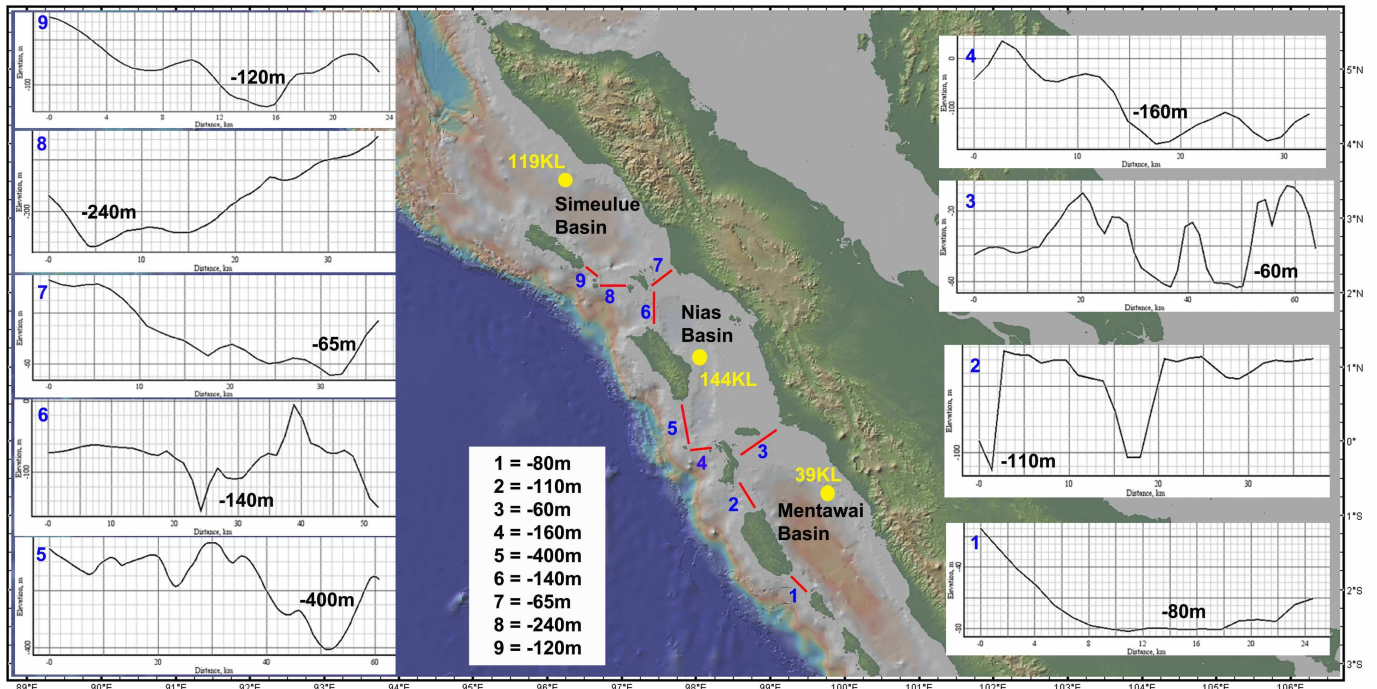
Extended Data Figure 1 | Instrumental records of temperature and precipitation in the study area. Records are at or close to the sites 119KL (black) and 39KL (red). **a**, Average monthly SST for the Simeulue basin (4°N, 96°E; black) and the northern Mentawai basin (2°S, 100°E; red) based on extended reconstruction sea surface temperature (ERSST) data from 1854 to 2008 (<http://nomads.ncdc.noaa.gov/las/getUI.do>). Dashed lines indicate average SST for the entire period. **b**, Twenty-four-hour air temperatures measured in Sabang in northwestern Sumatra (from 1976 to 1989; black) and in Padang in western Sumatra (from 1850 to 1989; red; <http://climexp.knmi.nl>).

Dashed lines indicate the average air temperature over the entire period. **c**, Average monthly precipitation (mm per month) over Banda Aceh in northwestern Sumatra (black) and Padang (red), between 1879 and 1989 (<http://climexp.knmi.nl>). Open circles represent mean monthly precipitation of different seasons (winter, spring, summer and autumn), with the numbers indicating the percentage contribution of each season to the total annual precipitation. Dashed lines indicate average monthly precipitation for the entire period. Note the small seasonality of SST, air temperature and precipitation in the study area.

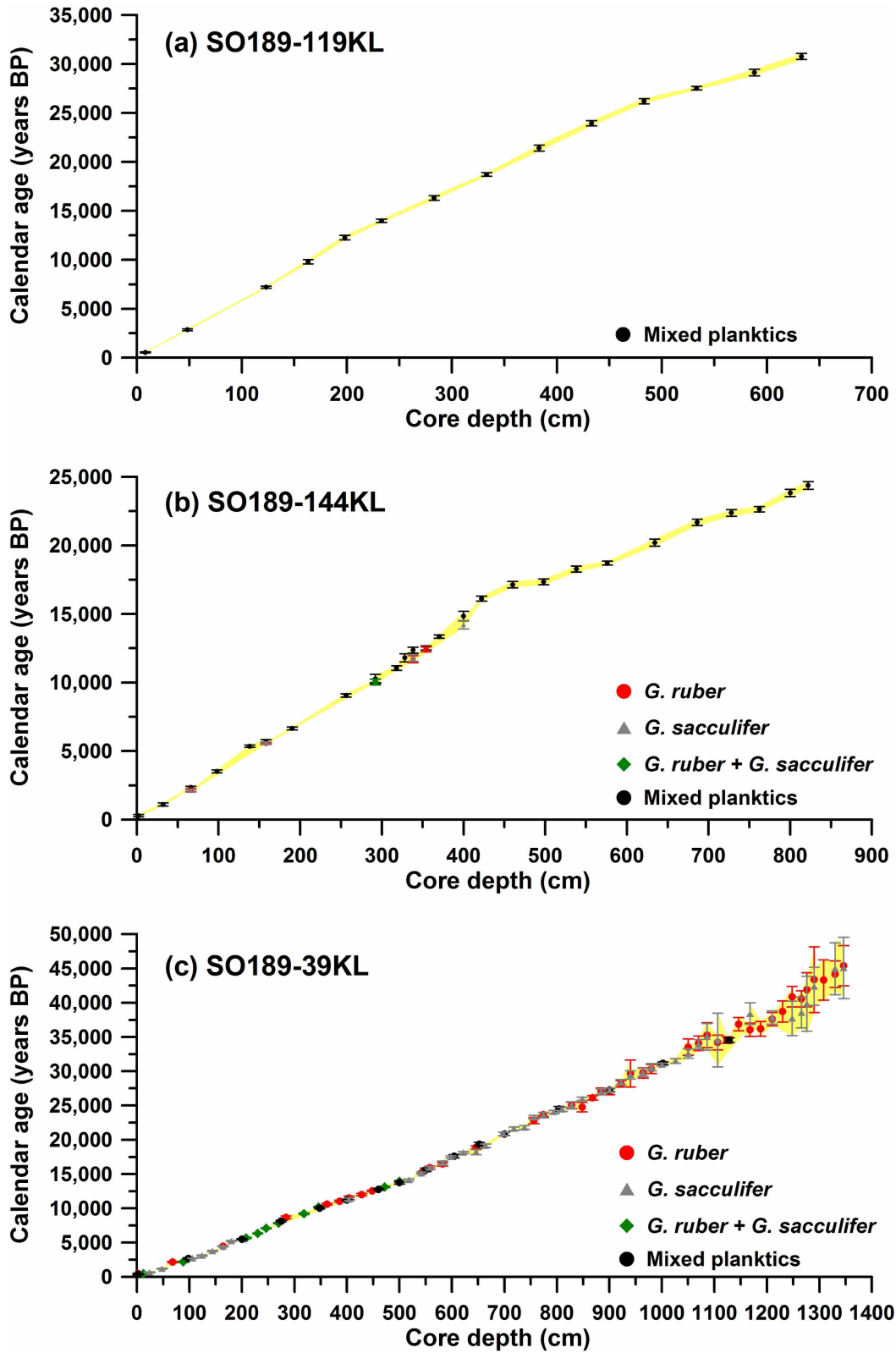


Extended Data Figure 2 | Seasonality of surface currents, SST and salinity in the eastern Indian Ocean. Seasonal changes in SST (colour shading), salinity (dashed lines; p.s.u.) and surface currents (arrows) in the study area during boreal summer (top) and winter (bottom). The meridional Ekman transport (ME) is also indicated with arrows. Seasonal SST is averaged for the period between 2002 and 2010 (<http://oceancolor.gsfc.nasa.gov/cgi/l3>). Salinities are averaged for the period between 1960 and 2004³¹. Surface currents and ME are

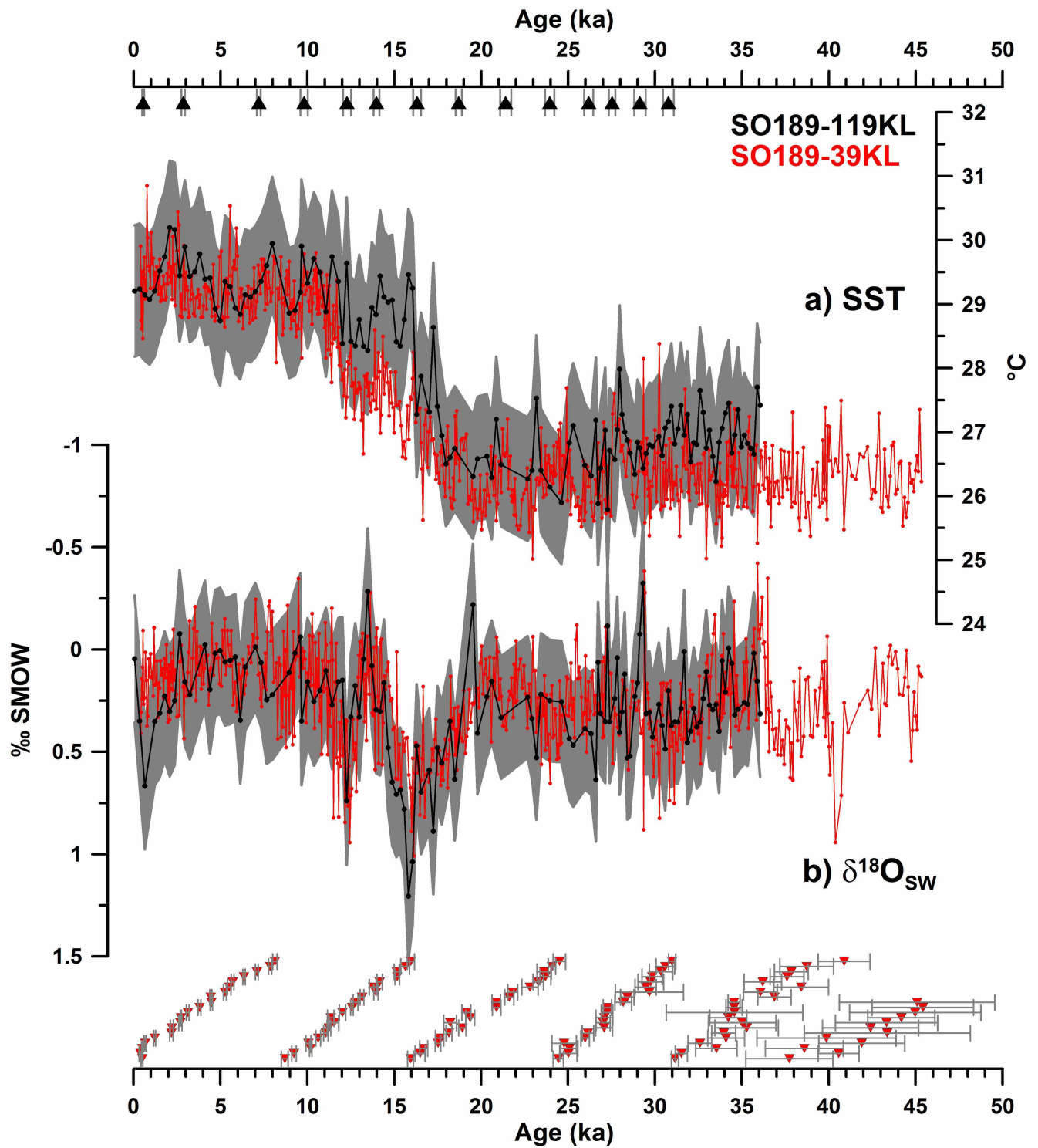
redrawn following ref. 35. Note the seasonal reversal of the surface currents and the MET, and the small seasonality of SST and salinity off western and northwestern Sumatra. The positions of the cores from the tropical eastern Indian Ocean are indicated by stars (this study). NECC, north equatorial counter current; NMC, northeast monsoon current; SECC, south equatorial counter current; SJC, south Java current; SMC, southwest monsoon current.



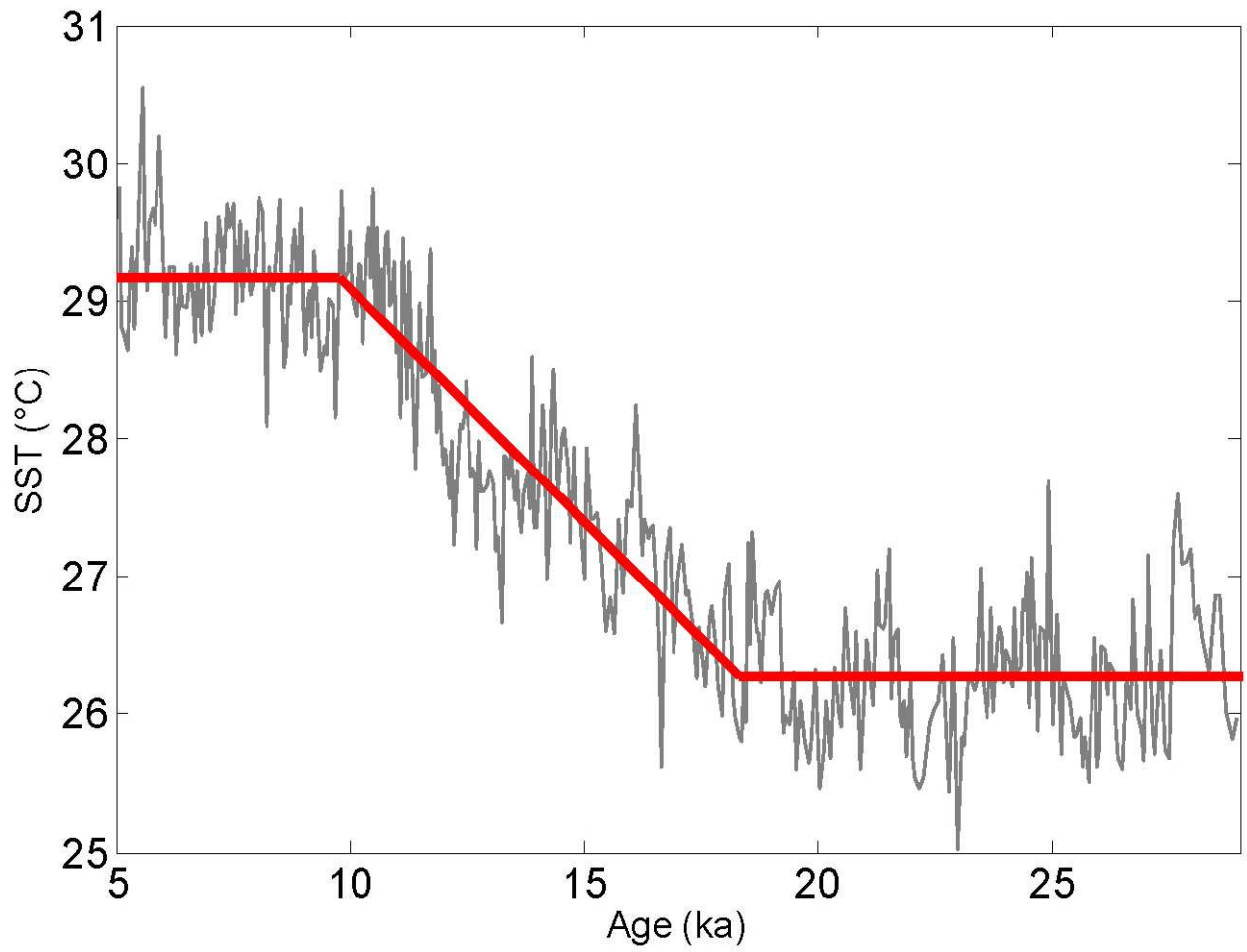
Extended Data Figure 3 | Sill depths in the study area. Sill depths of the Simeulue basin (1–3), the Nias basin (4–6) and the northern Mentawai basin (7–9), with the positions of the cores indicated (yellow dots). The maximum depth of each sill is as indicated.



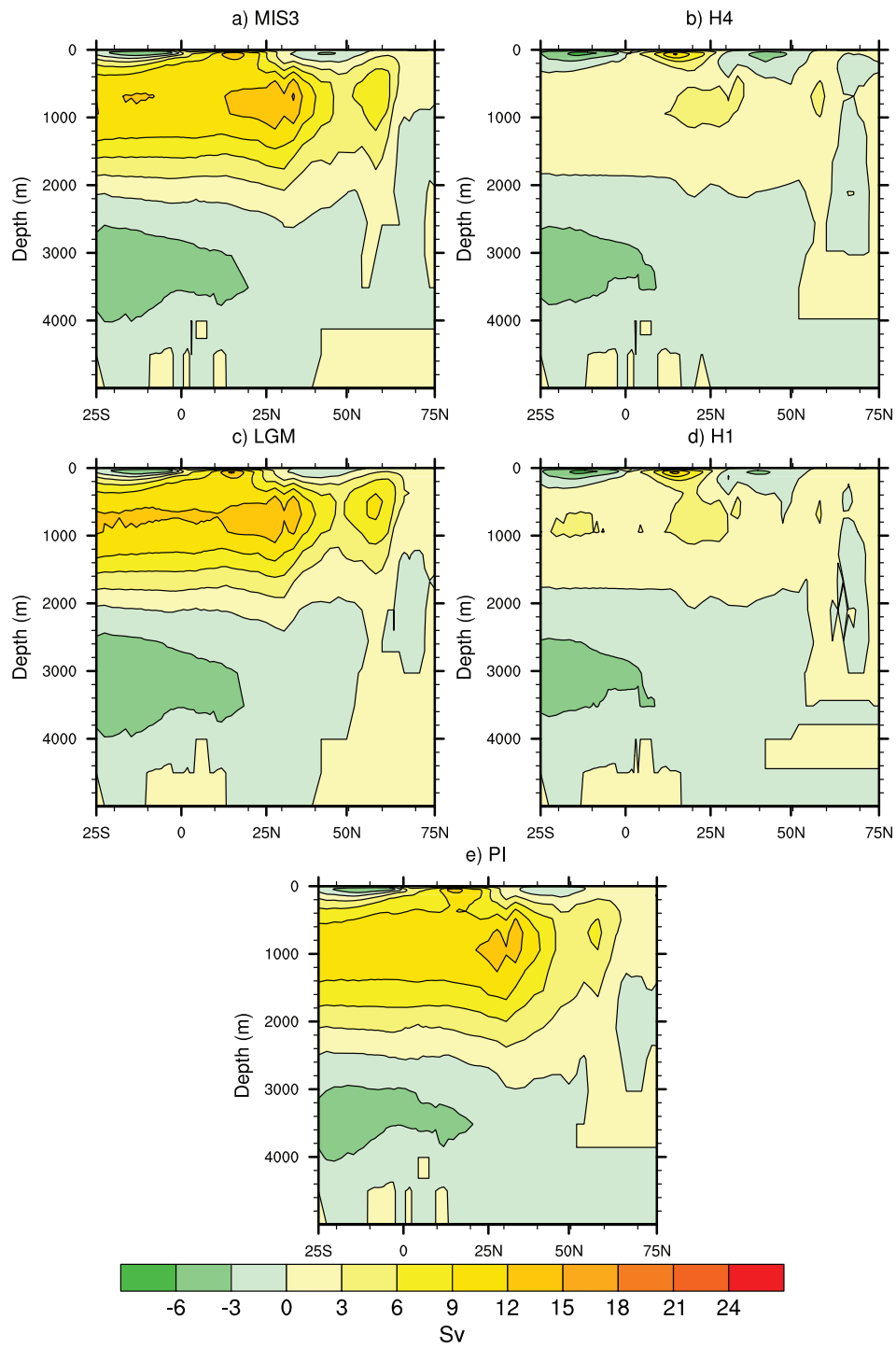
Extended Data Figure 4 | Age–depth relationship of the investigated cores. Core depth (cm) versus calendar age (years) with 2σ errors (bars and yellow envelope) in cores 119KL (a), 144KL (b) and 39KL (c).



Extended Data Figure 5 | Estimated errors (1σ) for SST and $\delta^{18}\text{O}_{\text{sw}}$ in core 119KL. Grey envelopes indicate errors in reconstructions of SST (a) and $\delta^{18}\text{O}_{\text{sw}}$ (b). For comparison, the 39KL records (red) are shown. Grey bars indicate 2σ errors of the calibrated radiocarbon ages (black and red triangles).

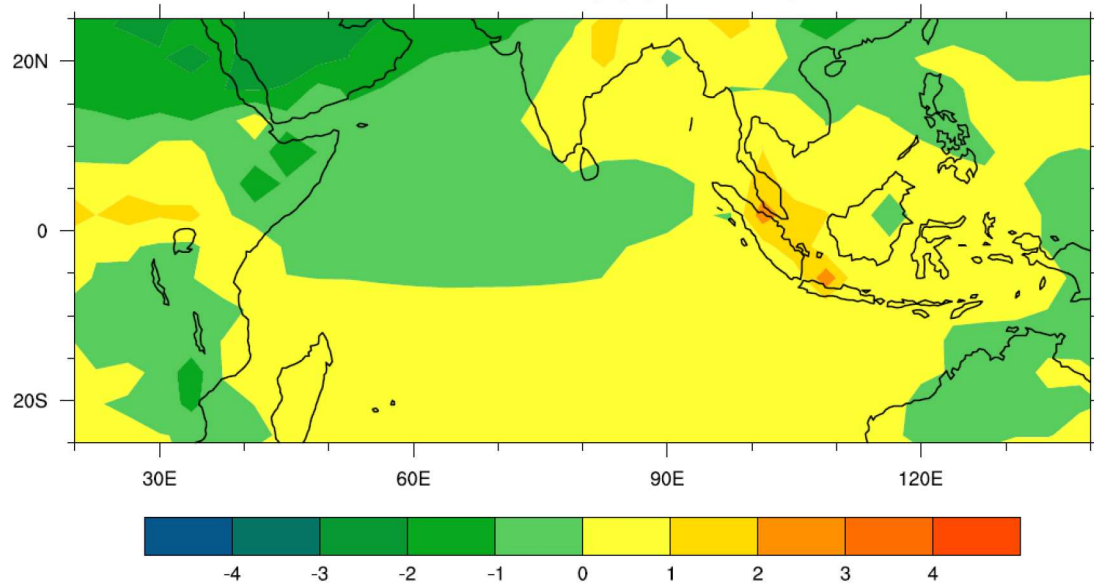
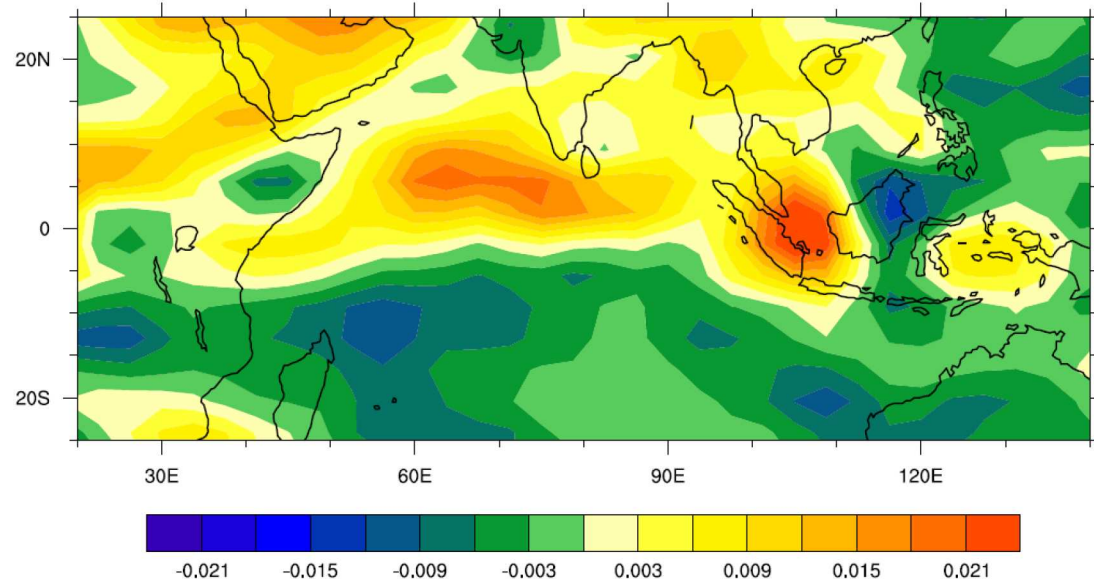


Extended Data Figure 6 | Mg/Ca SST record of core 39KL for the period 5–29 kyr ago, along with the fitted ramp function (red).



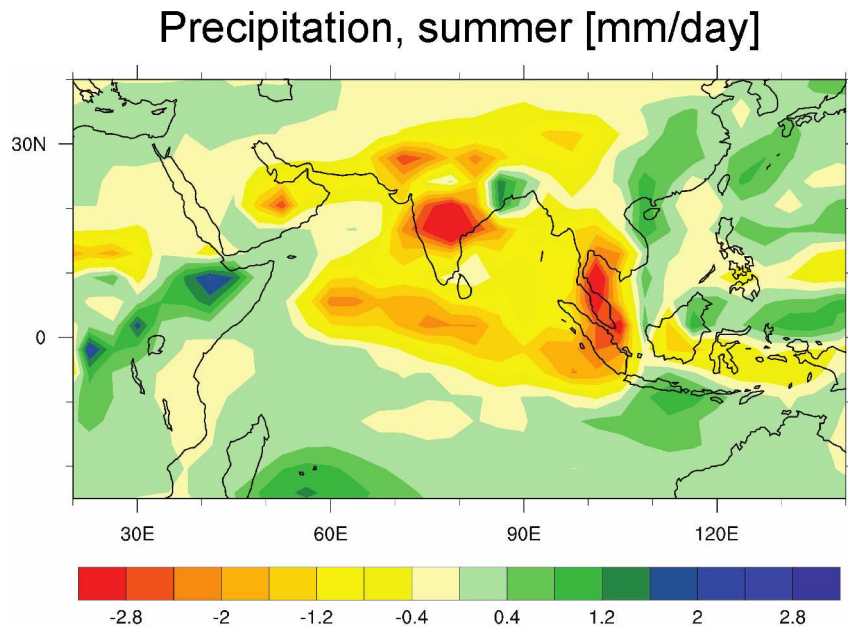
Extended Data Figure 7 | AMOC for different climate states, as simulated by CCSM3. Meridional overturning stream function averaged over the last 100 yr of each experiment for the MIS3 baseline run (a), the H4 hosing

experiment (b), the LGM simulation (c), the H1 hosing experiment (d) and the pre-industrial control run (e).

(a) Surface Temperature [$^{\circ}\text{C}$](b) Vertical Velocity at 500 hPa [Pa/s]

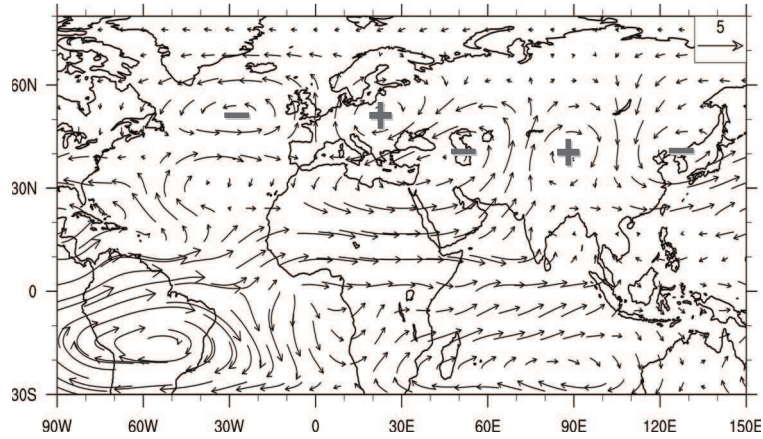
Extended Data Figure 8 | Climatic response to a substantial slowdown of the AMOC under LGM (21 kyr ago) boundary conditions in a CCSM3 simulation. Shown are long-term (100-yr) annual means of climatic anomalies

(Heinrich stadial 1 hosing experiments minus LGM baseline run) for surface temperature (a) and vertical velocity (b) at 500 hPa.

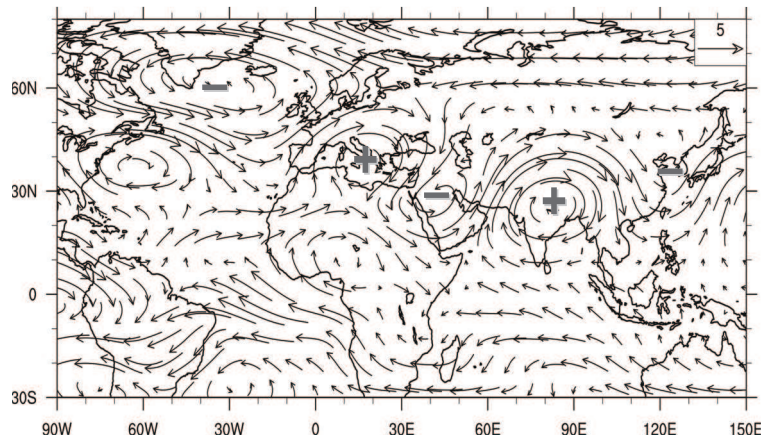


Extended Data Figure 9 | Summer (June, July and August) precipitation response to a substantial slowdown of the AMOC under MIS3 (38 kyr ago) boundary conditions, as simulated by CCSM3. Shown are 100-yr averages (Heinrich stadial 4 hosing experiment minus MIS3 baseline run).

(a) 200 hPa wind, summer [m/s]

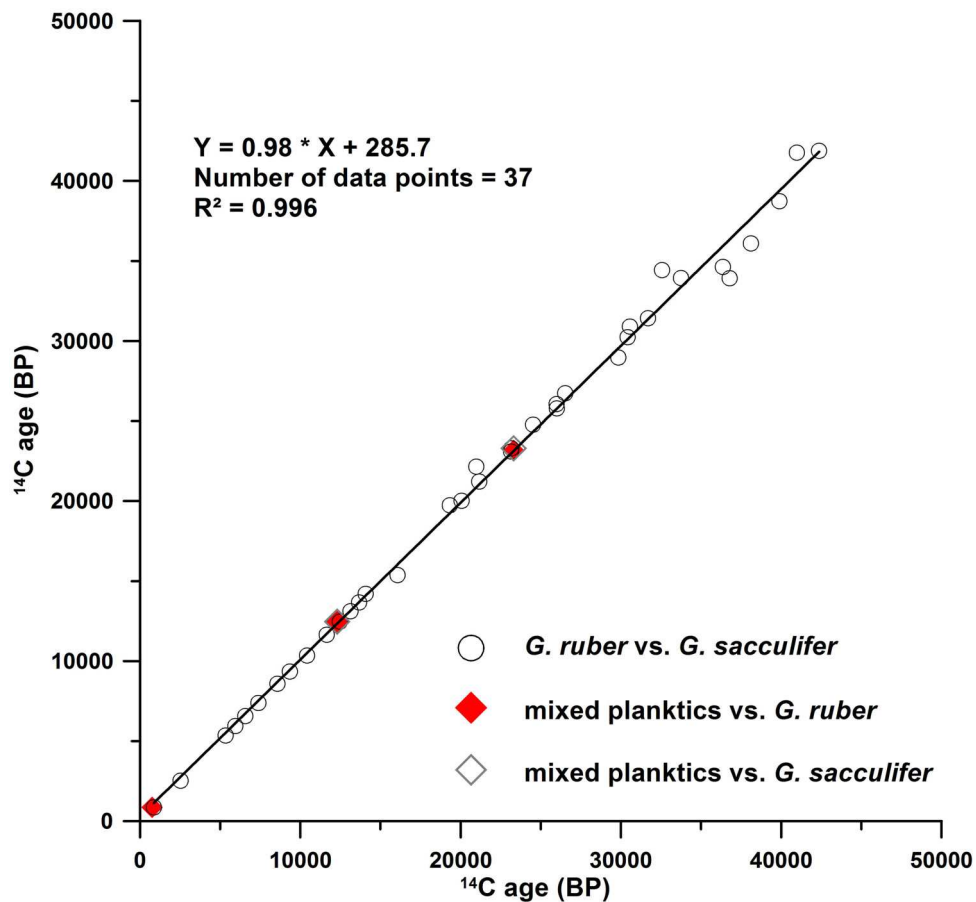


(b) 200 hPa wind, winter [m/s]

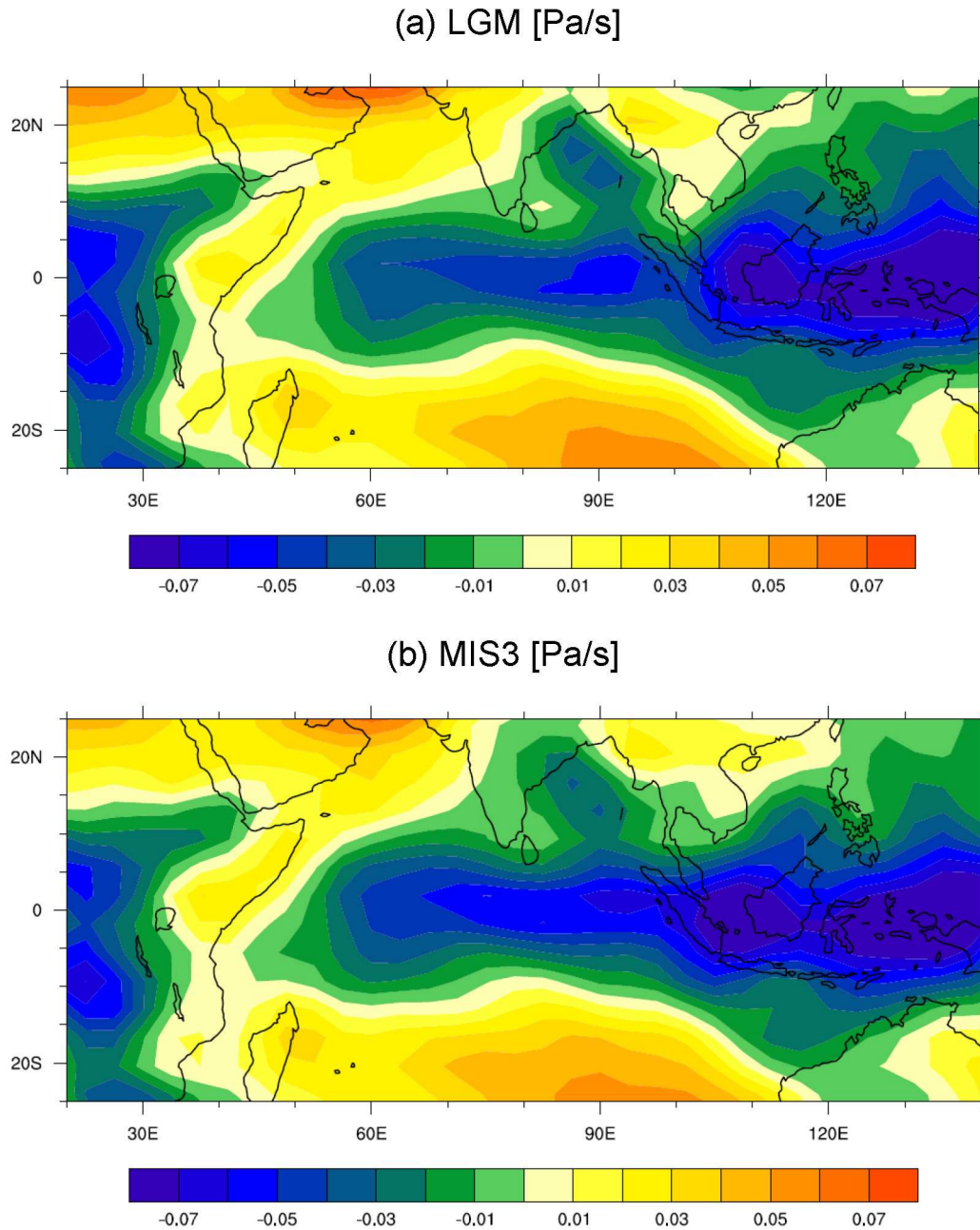


Extended Data Figure 10 | Upper-tropospheric (200 hPa) wind response to a substantial slowdown of the AMOC (Heinrich stadial 4 hosing experiment minus MIS3 baseline run; 100-yr averages). **a**, Summer (June, July and August) response; **b**, winter (December, January and February) response. Wave

trains are highlighted by plus symbols (positive geopotential height anomaly/anticyclonic circulation anomaly) and minus symbols (negative geopotential height anomaly/cyclonic circulation anomaly).

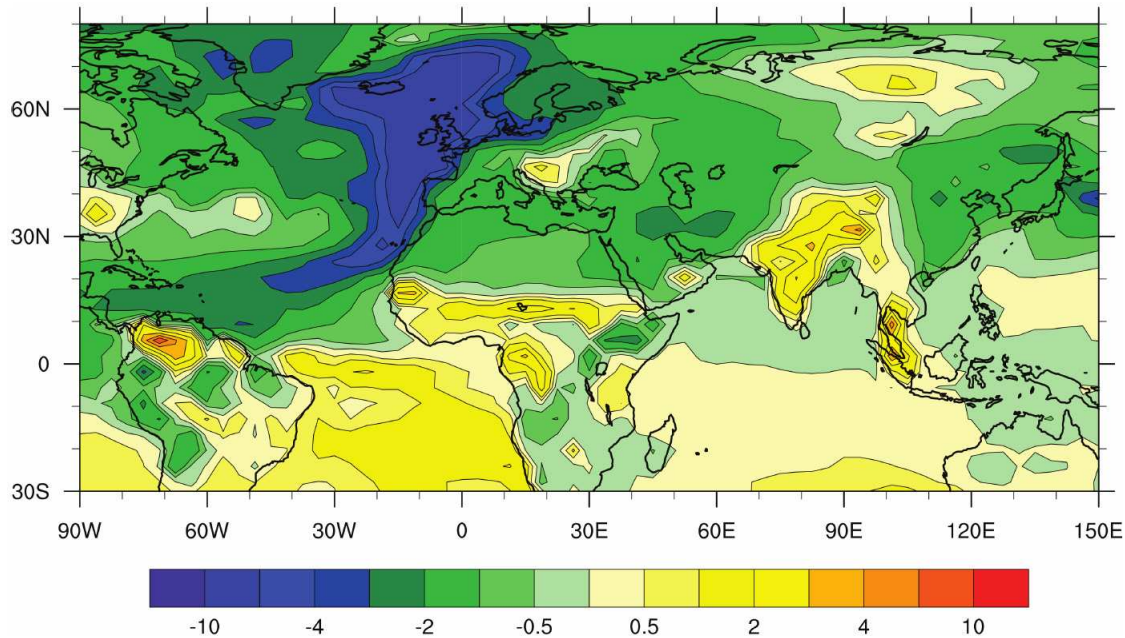


Supplementary Figure S1. Correlation between AMS ages in SO189-39KL measured on different species at the same depth.

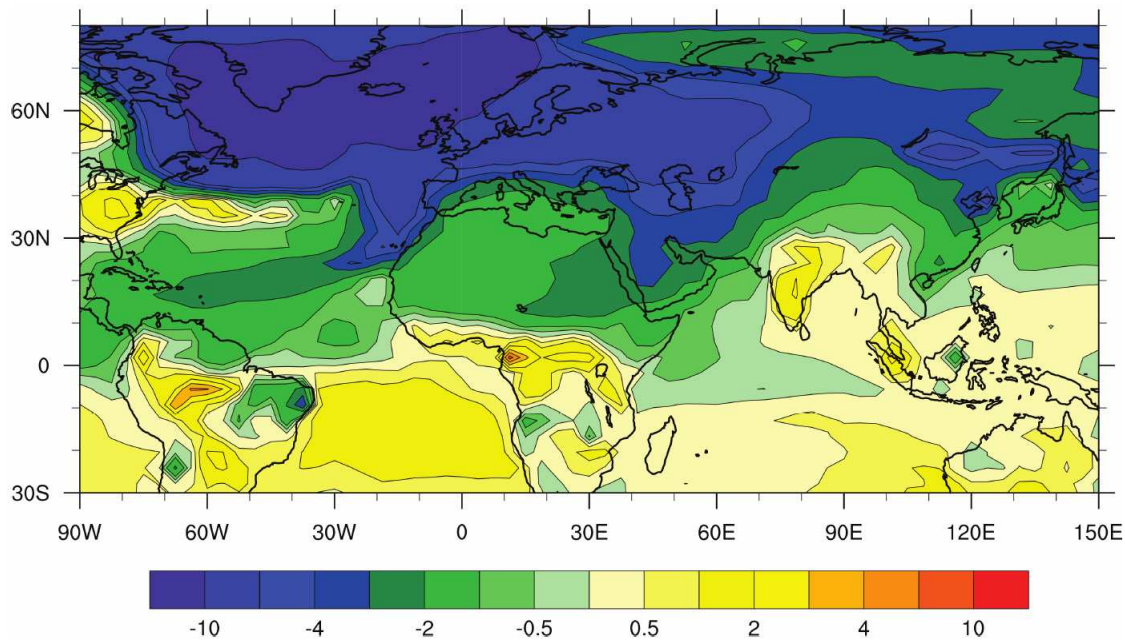


Supplementary Figure S2. Vertical velocity (ω) at 500 hPa over the Indian Ocean/Indonesian region as simulated by CCSM3 under glacial boundary conditions. Shown are long-term (100-yr averages) annual means for (a) the LGM (21 ka BP), and (b) the MIS3 (38 ka BP) baseline simulation.

(a) Surface temperature, summer [°C]



(b) Surface temperature, winter [°C]



Supplementary Figure S3. Surface temperature response to a substantial slowdown of the AMOC (H4 hosing experiment minus MIS3 baseline run; 100-year averages). Panels show (a) summer (June-July-August) and (b) winter (December-January-February) response, respectively.